Forschungszentrum Jülich GmbH - Institute for Energy Research

Microstructure and Properties of Materials (IEF-2)

RWTH Aachen – Institute of Ferrous Metallurgy

Influence of the thermomechanical treatment history on a Laves-phase hardened ferritic steel

Master thesis

Chichi Li
284103

Supervisor: Dr.-Ing Bernd Kuhn
Prof. Dr.-Ing Tilmann Beck
Prof. Dr.-Ing Wolfgang Bleck

May 2010

Acknowledgement

First of all, I would like to thank all the people that have helped me during the last few months. Without their help, this thesis could not be fulfilled successfully.

I would like to express my earnest thanks to Prof. Dr. L.Singheiser and Prof. Dr.-Ing. T.Beck for allowing me to carry out this work in the Institute for Microstructure and Properties of Materials (IEF-2). Meanwhile, I would also like to thank Prof. Dr.-Ing. W.Bleck for agreeing to be my external supervisor.

Furthermore I would like to express a deep sense of gratitude to Prof. Dr.-Ing. T.Beck and Dr.-Ing B.Kuhn, who guided me with immense patience. Thanks to the inspiring discussion sessions and their constant encouragement, this thesis was able to be accomplished successfully.

I would also like to express my sincere thanks to Harald Reiners, Horst Wershoven, Heinz Esser, Burkhard Werner, Volker Gutzeit, Jörg Bartsch, Egbert Wessel, Mario Schweda for their support in the experimental work. I am grateful to Leszek Niewolak, Thomas Eckardt, Mario Schweda for giving me lots of scientific ideas and suggestions.

I would like to thank all the staff of IEF-2 who helped me during my work period in our institute.

I take this occasion to thank my family and my friends for their support and for always standing beside me.

Abstract

The creep performance of the newly developed ferritic steel Crofer 22H at 600°C depends strongly on the processing and heat treatment history of the material. Microstructures of different batches of Crofer 22H with differing processing parameters and chemical compositions were examined and compared. Annealing experiments were used to determine the precipitation kinetics of different batches. Hardness tests were performed to determine the dislocation density of materials with different heat treatment history to investigate the change of dislocation density with heat treatment. Furthermore, stress relaxation and tensile tests were conducted to investigate the high temperature mechanical behavior of the batches as well as the influence of dislocation density change to the creep rate of the materials.

Content

1. Introduction

A new creep resistant ferritic steel (Crofer®22H, X1CrWNbTiLa22, W.-Nr.: 1.4750) developed by Forschungszentrum Jülich IEF-2 and ThyssenKrupp VDM shows promising results concerning future application in energy conversion systems like high temperature fuel cells. It shows excellent oxidation properties and resistance to creep deformation. With further optimization it may even be suitable for the application in advanced steam power plants in the temperature range from 600°C to 650°C.

However, during previous investigation, the first half-commercial batch unveiled mechanical behavior differing from the laboratory melts in the temperature regime that is interesting for steam power plants. The reason for this is assumed to be microstructural change due to the materials thermo-mechanical treatment that deviates from the laboratory melts. Dominating factors for the materials creep resistance like dislocation density and precipitation behavior as well as the dependency of these factors on chemical composition and thermo-mechanical treatment history are not yet fully understood.

This research aims to investigate the microstructural difference between the half-commercial material and the laboratory materials as well as to find out the influence of microstructural change on the mechanical behavior of the respective materials. Microstructural investigation with respect to grain morphology, precipitation kinetics and dislocation density was applied to 12mm slab material MGQ (sample material from the 20 tons half-commercial melt), 16mm slab material KUB and KSX (sample material from laboratory melts (~100kg)) to understand the intrinsic mechanism that caused different creep strength in these R+D-status steels. High temperature mechanical testing was applied to 2mm sheet materials MDO (from the same melt as MGQ), KUA (same melt as KUB) and KSY (same melt as KSX) to obtain more information concerning their high temperature mechanical behavior and to study the influence of cold working on mechanical property changes of this kind of steel.

During this study, precipitation behavior, grain size distribution and dislocation density were focused in the investigation of microstructure by optical and scanning electron microscopy as well as hardness testing, while in the mechanical test part, tensile- and stress relaxation tests were conducted.

Key words: Creep strength, ferritic steel, Laves-phase, dislocation density

2. Literature review

2.1 Steels for high temperature application (550~650°C)

The design lives of the pipework and other major components for electricity generating plants are usually 100,000 hours. The enormous range of properties which can be developed in steels has ensured their selection for large-scale structures for chemical and electricity generating plants.

Many of the critical components in modern power plants consist of tempered martensitic ferritic steel with 9-12% Cr. Typical laboratory heat treatments of tempered martensitic ferritic steels consist of austenitising (e.g. 1273 K, 1h, air cooling) followed by tempering (e.g. 1023 K, 2h, air cooling) treatment[1]. The temperature range during operation is between 773 and 923 K. However, microstructural degradation due to preferential recovery at the vicinity of prior austenite grain boundaries results in decreased creep strength, especially in the long term. The oxidation resistance of 9-12% Cr steels is insufficient as well. Both creep strength and oxidation resistance need to be improved in high-temperature structural materials to enable them to withstand higher steam temperatures and pressures[2].

To avoid the necessity to use more expensive austenitic steels or even Nickel-base alloys which also have disadvantages in their thermal and thermomechanical behavior (i.e. low thermal conductivity, high coefficient of thermal expansion), ferritic steels employing precipitation hardening by laves-phases are developed at IEF-2, Forschungszentrum Jülich as a possible alternative. For future application, further investigation needs to be conducted to gain better understanding of the creep behavior of this new steel.

2.2 Microstructure and strengthening mechanisms

2.2.1 Matrix types of steels

Typical steel matrices are ferrite, martensite and austenite stainless steel etc. The evolution of the matrix depends on the heat treatment procedures and the concentration of alloying components. The Schaeffler diagram[3], shown in Fig.1 presents the influence of different alloying elements on the stability of stainless steel microstructure.

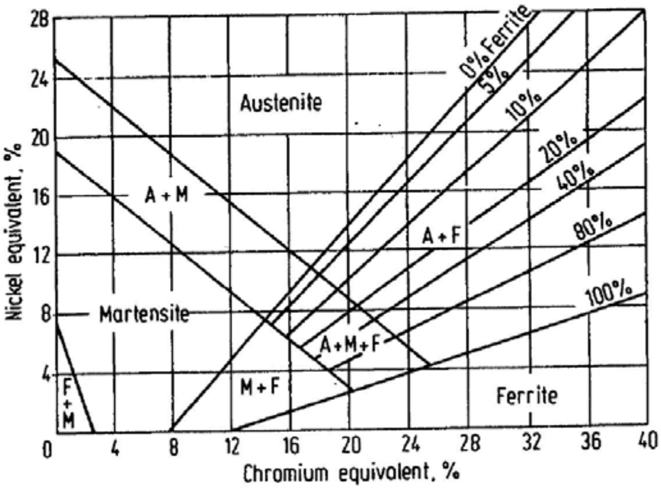

Fig.1 Schaeffler diagram [3]

The horizontal axis represents the Cr equivalent alloying content and the longitudinal axis the Ni equivalent alloying content. Chromium and some other elements, such as Mo, Si, Nb, Ti, are ferrite stabilizing elements, which have the effect of expanding the fraction of ferrite phase in parent austenitic phase. The quantified elemental effects are described by chromium equivalents, Cr_{eq}, shown in **Equation 1** [3]. In the opposite, Ni, C, Mn etc. are austenite stabilizing elements, which result in a higher fraction of austenitic phase what is quantified by nickel equivalents Ni_{eq}, shown in **Equation 2** [3].

$$Cr_{eq} = \%Cr + 2(\%Si) + 1.5(\%Mo) + 5(\%V) + 5.5(\%Al) + 1.75(\%Nb) + 1.5(\%Ti) + 0.75(\%W)$$

Equation 1 [3]

$$Ni_{eq} = \%Ni + \%Co + 30(\%C) + 25(\%N) + 0.5(\%Mn) + 0.3(\%Cu)$$

Equation 2 [3]

To investigate precipitation kinetics and dislocation movement, the matrix type of the steel is very important. It determines the solubility and diffusion rate of alloying elements, thus influences the kinetics. It is reported that after aging of a 15%Cr-ferritic steel, small, homogenously distributed intermetallic phases were found in the ferrite matrix while coarsened block-like particles precipitated sparsely within the martensite phases[4].

Furthermore a ferritic matrix is suitable for large and thick structural components that are exposed to high temperatures because of its low thermal expansion coefficient and high resistance to thermal fatigue[6]. Therefore further development of advanced ferritic steels seems to be a promising way.

2.2.2 Solid solution strengthening

Solid solution strengthening is a very important strengthening mechanism against creep. During creep, solute atoms can segregate to dislocations so that a greater stress is required to move the dislocation away from their solute atmospheres or, at temperatures where diffusion can occur, to drag the atmospheres along with the dislocation.

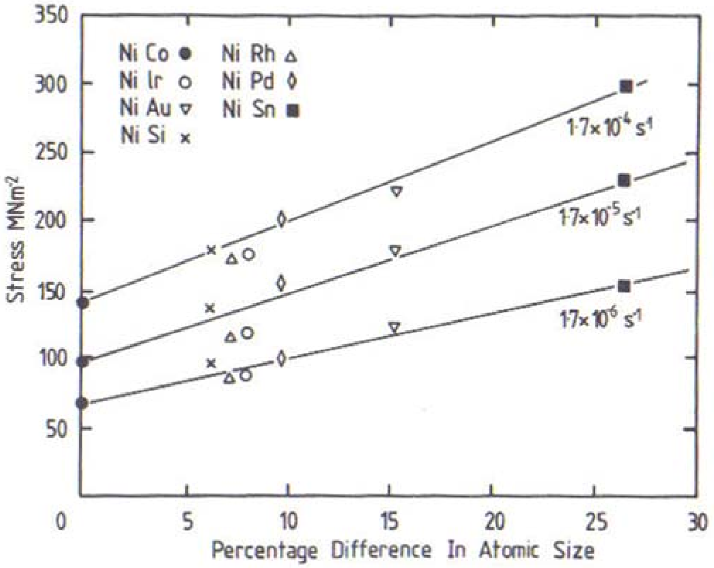

Fig.2 The relationship the percentage difference in atomic size of solute and solvent atoms and the creep resistance of various dilute nickel alloys tested at 773K[5]

There are several reasons for this kind of segregation[5], e.g. the strain field around a dislocation attracts solute atoms which are larger or smaller than the solvent atoms (usually termed elastic interaction or Cottrell locking); the rearrangement of the conduction electrons around a dislocation attracts solutes of different valency (normally referred to as electrical interaction); and the cohesive energy between atoms in a stacking fault differs from that for the matrix which results in a different equilibrium concentration of solute in the stacking fault and in the matrix (generally called chemical interaction or Suzuki interaction). Substantial improvements in creep resistance can be achieved by the addition of solutes which differ markedly in atomic size and valency from the parent metal. **Fig. 2** shows the secondary creep rate recorded for pure nickel and various dilute nickel alloys (containing only 0.1% solute) plotted as a function of the difference in atomic radius between nickel and the different solute additions[5].

For steels in high temperature application, Nb, W and Mo are typical solid-solution strengthening elements. Especially Nb was reported to improve the high temperature strength effectively[6]. As can be seen from **Fig. 3**, in 13Cr steels with the increase of Nb content in solid solution (**Fig.3 b**), the 0.2% proof strength at 900°C increases significantly (**Fig.3 a**). Compared to Nb, Mo also improves the high temperature strength, but only approximately in proportion to the addition content.

However, other than in solid solution state, Nb is also an important precipitate-forming element. Because of the high reactivity of Nb with C and N, niobium carbonitride easily forms in some processing stages, e.g. in hot-rolling and annealing processes. As a result, the content of Nb in solid solution would be reduced and in turn cause a degradation of the initial strength. It is reported that high temperature strength of Nb added 13Cr steels decreases during high temperature aging and it is caused by coarse Fe_3Nb_3C formation[6]. From **Fig. 3 c** and **d** it is obvious that it is the Nb in the solid solution state that contributes to the initial strength increase rather than that in the precipitation state.

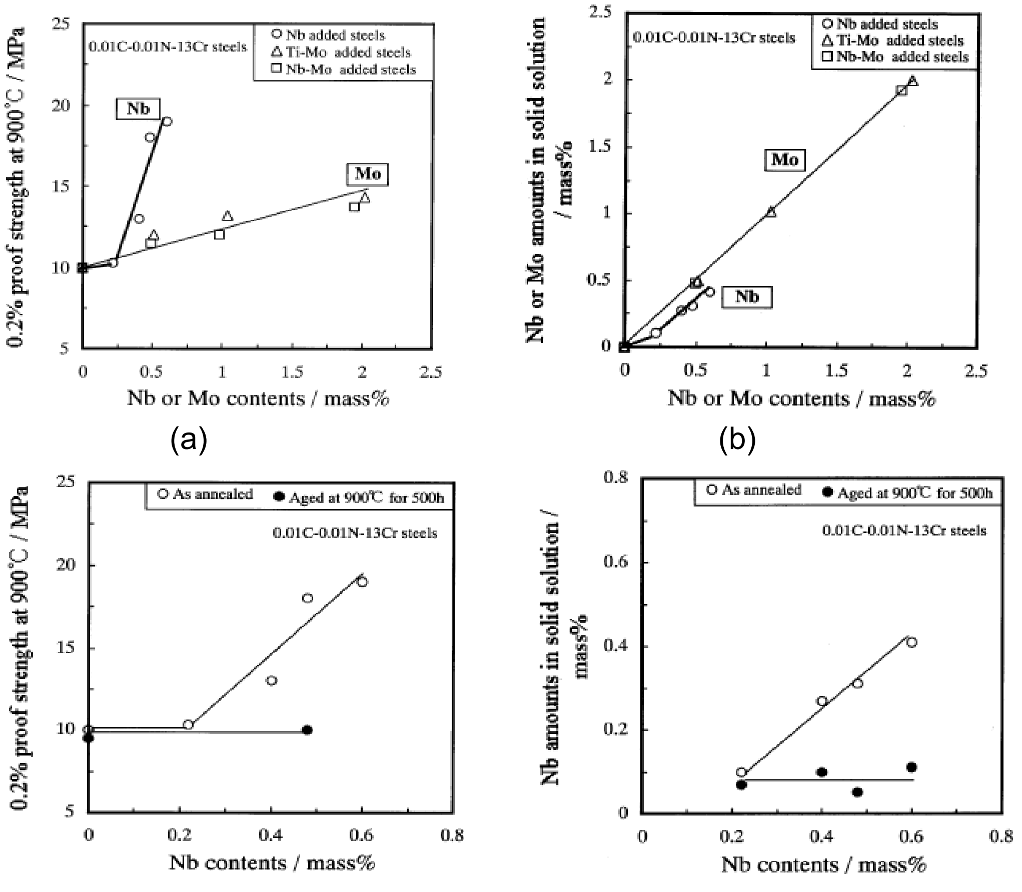

(a) (b)

(c) (d)

Fig.3 Influence of Nb to high temperature initial strength of 13Cr steels[6]

In order to obtain the best high temperature mechanical properties, lots of efforts were made to find balances between solid solution strengthening and precipitation strengthening stages. Investigation showed that addition of Ti and Mo can control the precipitation process in Nb alloyed ferritic stainless steels, Fe_2Nb forms instead of Fe_3Nb_3C which has slower nucleation and growth rate[6].

2.2.3 Precipitation behaviour at high service temperature

2.2.3.1 Influence of precipitate size and distribution on creep properties

While solid solution elements strengthen the steel by increasing the threshold stress which is necessary to start the dislocation movement in the plastic deformation regime, precipitates harden the steel mainly by obstructing the dislocation movement.

In high temperature deformation, the dislocation movement depends on the applied stress. At high stress levels, the dislocations circumvent the precipitates by passing through while at low stress levels, the dislocation can also overcome the obstacle by climbing.

If precipitate particles can be intersected depends on their crystal structure too. The phase boundaries of incoherent precipitates act on dislocations like grain boundaries and are insurmountable obstacles. Dislocations can only circumvent incoherent precipitates by the so called Orowan mechanism*. For coherent or partially coherent precipitates, dislocations are capable of cutting through such a precipitate, only with smaller forces to overcome than that needed for the Orowan mechanism[20].

To obtain the optimal strength by pinning, the size, volume fraction and distribution of the precipitates is of extreme importance. **Fig.4** shows the variation of the secondary creep rate with particle spacing for copper-cobalt alloys[5]. When the particles are too small, dislocations can cut through the precipitates, however, with increasing particle size, the stress needed for the dislocations to cut through increases gradually, so the creep rate decreases accordingly. When the size and spacing of the precipitates reach a critical size, the dislocations are able to bow between rather than cut through the precipitates. At this point, the creep rate reaches the minimum value and the strengthening of the precipitates become optimal. Above this critical size, the creep rate then increases as bowing becomes progressively easier with increasing particle size and spacing. Nevertheless, it is difficult to tell the optimum particle size and spacing for a certain material because it depends on various parameters, such as precipitate/matrix phase structure, stress dependent dislocation movement etc.

* Orawan mechanism: When a dislocation passes through a particle with incoherent phase boundary, the dislocation circumvents the particle by forming a dislocation loop around the particle and a free dislocation that can move on.

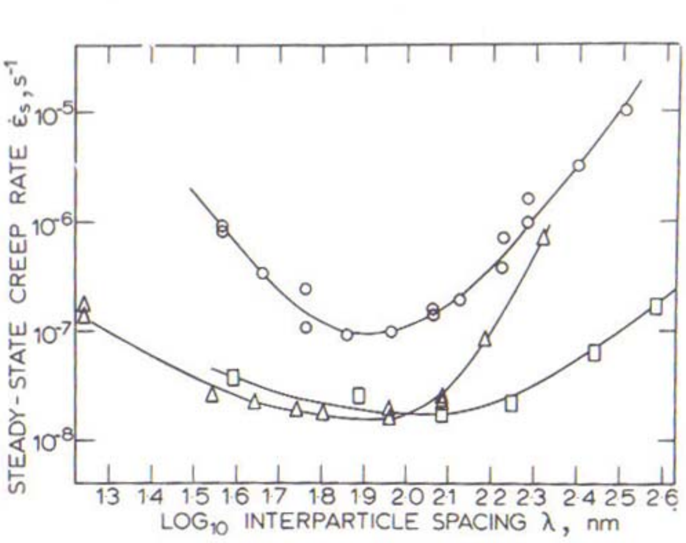

Fig.4 The variation of the secondary creep rate with particle spacing for copper-cobalt alloys containing 0.88%Co (○), 2.48%Co (Δ) and 4.04%Co(□) tested at 77.2MNm^{-2} and 712K[5]

2.2.3.2 Types of precipitates in creep resistant steels

Typical precipitates in creep resistant steels are carbides, nitrides in the form of (MX) and laves-phases[7]. Precipitates that were discovered in the current investigation are mainly the following:

MX (M-metal, X- C, N):

Typical MX forming elements are V, Nb, Ti and Ta. Among these elements, Ti has the highest affinity to C and N and forms TiN which is extremely stable up to the melting temperature of the steel. It is reported that MX precipitates form easily in ferritic matrices with Ti % > 0.002wt. % [7].

Plenty of parameters have to be controlled to give the desired material quality. Namely these controllable measures are chemical composition, purity of pre-materials, processing parameters etc. Therefore, it should be pointed out that because of the high stability of the MX precipitates, it is difficult to control its precipitation behavior by specific heat treatment, which limits the targeted usage of this kind of precipitates for strengthening purpose.

Laves-phase:

The laves-phase is an intermetallic compound of A_2B-type with topologically close packed (TCP) structure and is expected to have good high temperature stability[8]. Recent development showed that precipitation of a mixed laves-phase $(Fe,Cr)_2(Nb,W)$ significantly improved the creep strength of a high Cr-ferritic steel at 700 and 800°C[9]. Typical laves-phase forming elements in steels are Mo, Ta, Ti and W[8].

Hättestrand et al. used APFIM (Atom Probe Field Ion Microscopy) to measure the volume fraction of laves-phase in a 9%Cr-steel and results showed that the growth of laves phase precipitates takes place during the first 10,000 h of ageing. During this process a matrix depletion of tungsten and molybdenum and thereby a decrease in solid solution hardening takes place. This loss of strength can to some extent be compensated by precipitation hardening if the number density of laves-phase precipitates is high enough[10].

Si plays an important role in the formation and growth of laves-phase particles. Hosoi et al. reported that elimination of Si suppresses the precipitation of the laves-phase in ferritic matrices[11]. It was shown that a decrease of the Si content from 0.67 to 0.008 wt.% strongly increases the time required for laves-phase formation (at 900K: from 10 ks to 500 ks; time intervals taken from Fig.9 in [11]). It was also suggested that laves-phase particles do not reach thermodynamic equilibrium as they form and grow during long term creep (120 MPa, 823 K, 139971 h) of a 12% Chromium tempered martensitic ferritic steel due to the slow diffusion of Silicon ($D_{Si}^{\alpha}=9.7*10^{-21}$ m^2/s calculated from TCFE6 and MOB2 databases using Thermocalc) in the steel matrix when incorporating into the laves-phase[12].

Sigma phase:

Because of the recent tendency of increasing the service temperature of heat resistant steels, more chromium was added to the steels in order to increase the steam corrosion resistance of steels for high temperature application. However, this high content of chromium on the other hand can lead to enhanced Sigma phase formation. The sigma phase was observed to appear after long term creep at temperatures of ~650°C in the form of Cr_7Fe_8. Because of its brittle nature, it may be critical in thermal cycling and thermomechanical fatigue and may increase the fracture susceptibility as well[30,31]. Therefore its appearance is usually considered to be disadvantageous to the long term application of creep resistant steels. **Fig.5** shows its typical morphology and distribution. These pictures were taken from a high tungsten laves-phase forming model alloy developed at IEF-2, FZ-Juelich with a chromium content of 22% for the application in high temperature fuel cells. The Cr-content of this model alloy is considered to be too high for application in the 600°C to 650°C temperature regime because of pronounced σ-phase formation.

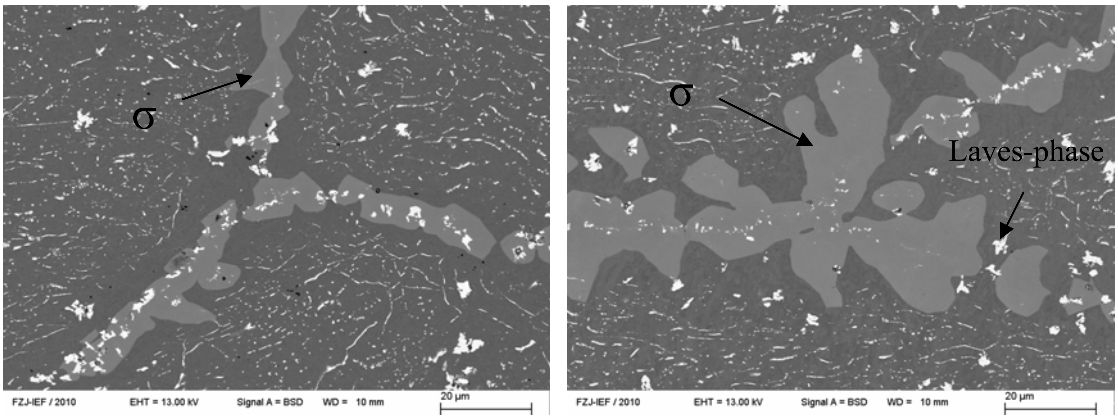

Fig.5 Typical morphology and distribution of the sigma phase (high tungsten laves-phase forming model alloy developed at IEF-2, FZ-Juelich, 700°C-25MPa, 5137h)

2.2.3.2 Interaction between different precipitates:

Both simulation by Thermo-Calc[7] and experimental investigation[13-14] show that copper has a low solubility in a ferrite matrix and forms a separate Cu-rich precipitate. However, this copper-rich precipitates do not contribute to long term creep strength because of their fast coarsening rate, but they work as nucleation site for the laves-phase. The accelerated nucleation leads to higher number density and smaller particle size of the laves-phase. Experimental results[13] showed that after growth at 600°C the final diameter of laves-phase particles is ~140 nm in P122 (with Cu particles) compared to ~280 nm in P92 (without Cu particle) while the volume fraction of the laves-phase in the two steels is the same. This means that the contribution of the laves-phase to creep strength is larger in steels with Cu particles compared to those without.

Coarsening rates of different precipitates also vary in different steels because of the interaction between them. It was reported that rapid precipitation and coarsening of the laves-phase reduces the coarsening rate of $M_{23}C_6$ in the matrix. On the other hand, the growth rate of the laves-phase was observed to be higher than the coarsening rate of the laves-phase in the steel without $M_{23}C_6$ precipitates[15].

Luntin et al. analyzed the atom concentration of different elements in laves-phases and in the surrounding matrix[16]. It was found that carbon, phosphorus and silicon were localized well inside the laves-phase precipitates while phosphorus and silicon were rejected from $M_{23}C_6$. Thus supposition was made that rejected silicon and phosphorus segregate and act as nucleation sites for the laves-phase. This theory was also experimentally supported by the observation of laves-phase nucleation in the form of thin sheets around $M_{23}C_6$ precipitates in 9Cr-1Mo steel.

2.2.4 Influence of dislocations on high temperature mechanical properties

When dislocation creep processes become dominant, dislocation density and its interaction with precipitates plays an important role in maintaining the creep strength of the material. Typical values for dislocation densities in pure metals and alloys are 1×10^{12} m^{-2} (undeformed) and 1×10^{16} m^{-2} (after severe cold working)[17]. Martensitic ferritic steels do have high density of dislocations caused by the martensitic phase transformation during tempering. For pure ferritic steels without phase transformation feasible, possible ways of introducing dislocations into the matrix is either by severe plastic deformation.

There are several methods to quantify the dislocation density in steels. Commonly the evolution of dislocation densities is analyzed by transmission electron microscopy (TEM) and X-ray diffraction (XRD). TEM gives information on dislocations on a micro scale while XRD quantifies dislocation density of the material in an overall view.

An indirect measurement of the dislocation density can be performed by hardness testing. Since the intrinsic hardness of the metal arises from the dislocation density of the matrix, it can be expressed by the **Equation 3** as follows:

$$H_0 = 3\sqrt{3}\alpha\mu b\sqrt{\rho_s} \qquad \textbf{Equation 3*}$$

Where α is a constant, μ is the shear modulus and b is the Burgers vector.

*It should be specifically mentioned here that this equation only gives the relationship between the intrinsic hardness and the dislocation density. It should be noticed that there are also other factors that could affect the intrinsic hardness such as solid solutes, precipitates etc. Therefore, the deduced dislocation density by this equation would not be very precise and should be further proved by other measuring methods.

With the equation above, by measuring the intrinsic hardness the dislocation density of the objective metal can be calculated. However, because of the indentation size effect (ISE), it is difficult to measure the intrinsic hardness simply by ordinary indentation testing. The well-known indentation size effect for metals means that the hardness increases with decreasing indentation size, especially in the sub-micrometer depth regime.

Nix et al. built a model for the indentation size effect in which this phenomenon was understood in the following way: Large strain gradients inherent in small indentations lead to geometrically necessary dislocations that cause enhanced hardening[18]. **Fig.6** schematically shows the geometrically necessary dislocations used in the Nix-Gao model. According to this simplified structure, the authors deduced a simple expression to relate hardness with indentation depth:

$$\left(\frac{H}{H_0}\right)^2 = 1 + h^* \cdot \left(\frac{1}{h}\right)$$ **Equation 4**

Where h* is a characteristic length that characterizes the depth dependence of the hardness. By measuring the hardness change with indentation depth, the intrinsic hardness Ho can be calculated. Combined with **Equation 4**, the dislocation density can be calculated as:

$$\rho_s = \frac{Ho^2}{27\alpha^2\mu^2b^2}$$ **Equation 5**

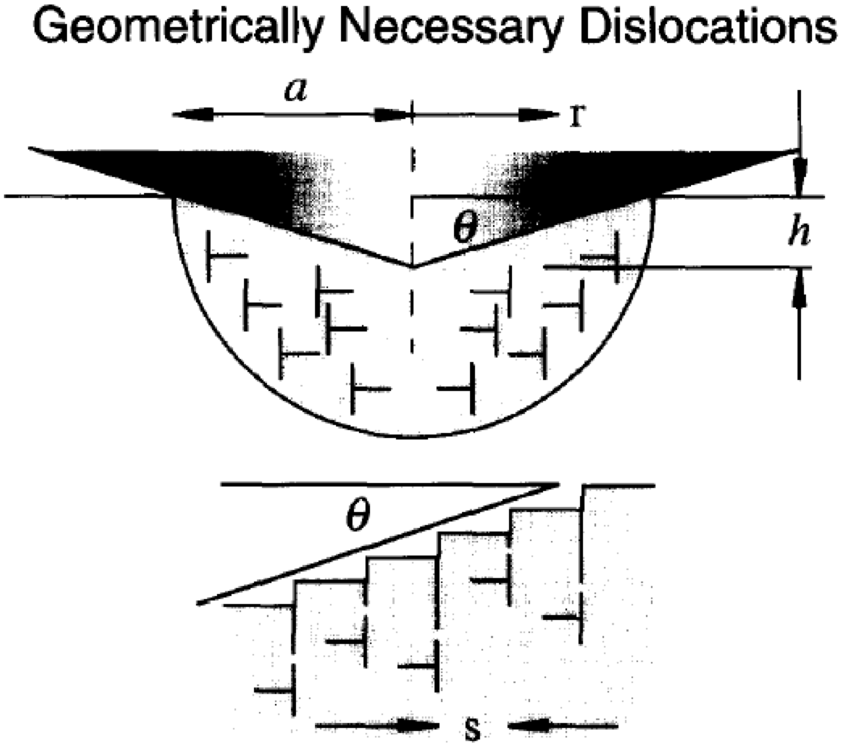

Fig.6 Geometrically-necessary- dislocations created by a rigid conical indentation. The dislocation structure is idealized as circular dislocation loops.

Graca et al. further proved this model by comparing the estimated value of dislocation density from indentation hardness measurement with those obtained by TEM in a laser clad Ni specimen, where the results showed consistency[19].

Although this method of measuring the dislocation density might not have high absolute accuracy, it gives a rough impression of the dislocation density of certain materials. Despite the facts that sample preparation and the measuring procedure are more convenient, it is faster and cheaper than other methods such as TEM and XRD measurement.

2.2.5 Influence of grain size and grain morphology on high temperature mechanical properties

In contrast to low temperature deformation in which grain refinement is treated as strengthening mechanism, it is widely accepted that fine grains are detrimental to the high temperature creep strength of a material. The creep rate increases with decreasing grain size in fine-grained material[20]. The main reason for the degradation of creep resistance with smaller grain size is accelerated grain boundary sliding because of larger grain boundary area.

Lai et al. found that the creep rate was reduced as the mean linear intercept grain size* was increased from 50μm to 140 μm[21]. However, it was also reported that the steady state creep rate was essentially independent of the grain size for coarse grain sizes (greater than or approximately equal to 100μm) while it increased with a decrease in grain size at finer grain sizes[22]. Despite of the various different versions of the dependency of creep strength on grain size, it is believed that the dependency is different for different materials and needs respective focus and investigation for every single material.

* Mean linear intercept grain size: This standard intercept count method of ASTM E112 has been developed to estimate planar grain size in an efficient and unbiased manner. It is based on the number of grain boundary intersections per unit length P_L through a random test line. The mean linear intercept length L can then be derived as: $L = P_L^{-1}$, which is denoted as the average distance between grain boundary intersections along the test line. From basic assumptions regarding grain shape, grain sampling and grain size distribution type, L is assumed to be directly proportional to the three-dimensional spatial grain diameter D[23].

2.3 Mechanical high temperature testing

2.3.1 Creep testing

When a stress is applied to a metal or alloy, after the virtually instantaneous strain which occurs on loading, the material may continue to deform in a time-dependent manner and may eventually fail. This phenomenon, known as creep, can virtually occur at all temperatures above absolute zero, but become more significant with increasing temperature.

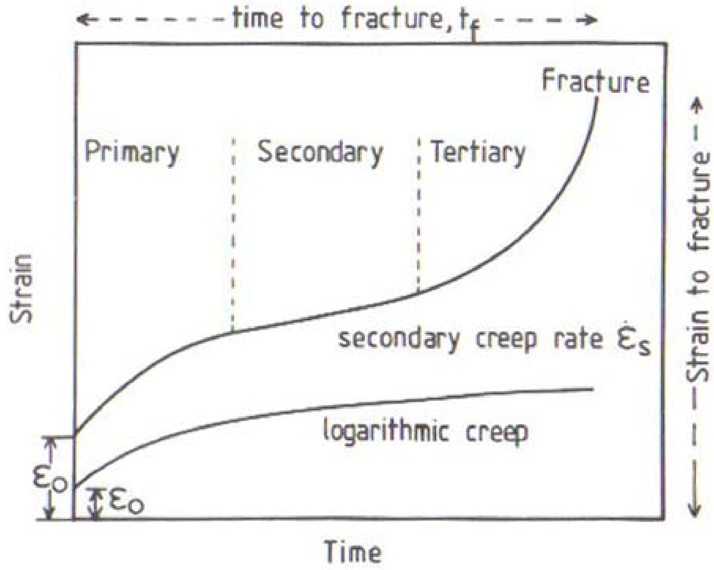

Fig.7 Typical curve of logarithmic creep and normal creep[5]

Generally, short term creep tests up to about 100 hours duration are normally undertaken for material quality assurance while long term tests are conducted to obtain design data[5]. Typical creep curves of logarithmic creep and normal creep are shown in **Fig.7**. In the low temperature regime ($\leq 0.4T_m$, T_m is the melting temperature of the corresponding material) logarithmic creep takes place, in which the creep rate falls continuously with time and the deformation processes occurring do not lead to fracture. However, as the temperature rises towards $0.4T_m$, after attaining the instantaneous strain ε_0, the primary stage follows in which the creep rate decreases continuously. Eventually the creep rate would become constant which is caused by a balance between the rate of generation of dislocations and recovery processes. This period is defined as the secondary creep stage. Nevertheless, lots of materials do not show extended secondary stages with constant creep rate but display only a short period of minimum creep rate. When it comes to the tertiary stage, the creep rate increases again till fracture occurs[5].

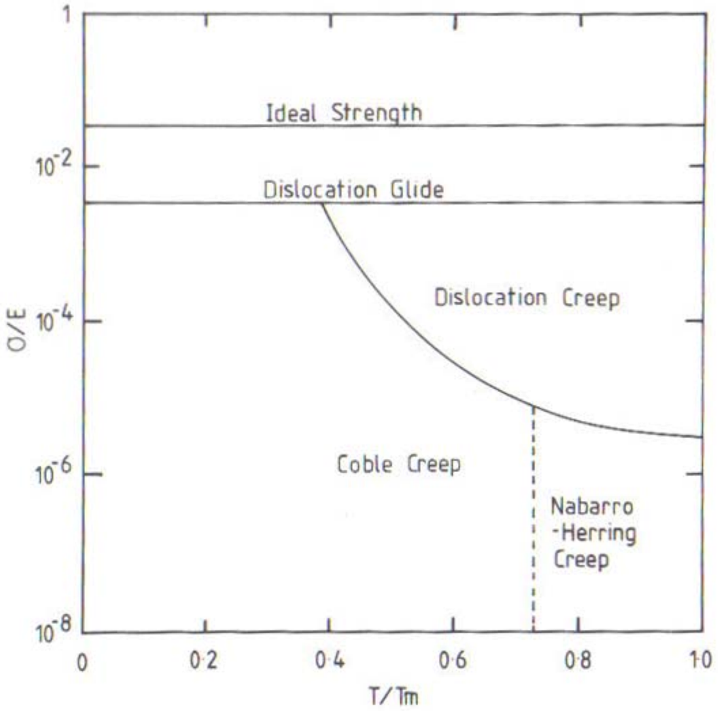

Fig. 8 Deformation map for a polycrystalline metal[5]

Creep properties displayed by a material differ in different temperature/stress regimes. For engineering convenience, deformation mechanism maps were developed which present the deformation characteristics of a material in the form of a stress/temperature diagram (**Fig.8**). As can be seen from the diagram, under different stress and temperature, either diffusion creep (Nabarro-Herring creep and Coble creep) or dislocation creep can be dominant. The creep rate during diffusion creep is proportional to the applied stress. For Nabarro-Herring creep, the creep rate is also considered to be proportional to the bulk self-diffusion coefficient and can be expressed in the following equation:

$$\dot{\varepsilon}_{NH} = A_{NH}\left(\frac{D}{kT}\right)\sigma\frac{\Omega}{d^2}$$ **Equation 6**

Here $\Omega \approx b^3$ is the atomic volume and d is the grain size. A_{NH} is a constant. From **Equation 6** and **Fig.8**, it is obvious that Nabarro-Herring creep strongly depends on temperature and grain size. The smaller the grain size, the higher the creep rate.

At lower temperature and in fine-grained materials, the rate of atomic transport along grain boundaries can exceed volume diffusion and dominate diffusion creep. In this case, the diffusion creep is referred to as Coble creep:

$$\dot{\varepsilon}_{C} = A_{C}\left(\frac{D_{GB}\delta}{kT}\right)\sigma\frac{\Omega}{d^3}$$ **Equation 7**

Where δ is the thickness of a grain boundary and D_{GB} is the coefficient of grain boundary diffusion. As can be seen from this equation, grain size has a bigger influence on Coble creep than on Nabbarro-Herring creep.

For dislocation creep, the stress dependence of the steady state creep rate follows a power law, which is called the Norton's Law:

$$\dot{\varepsilon}_{s} = B\sigma^{n}$$ **Equation 8**

The value of n can vary from ~3 to as high as 40 for various alloys at different conditions. This n value can be determined experimentally from the slope of the $\log\dot{\varepsilon}_s/\log\sigma$ relationship for a material tested at constant temperature and usually implies the corresponding deformation mechanism at the respective conditions. Normally, dislocation creep processes are associated with stress exponents of three or higher, whereas an n value of ~1 would be expected for the diffusional creep processes[5]. Even for dislocation dominated creep processes, different n values represent different ways of dislocation movement. Tjong et al. [24] reported that for the solid solution alloy Fe-19Cr-4Ni-2Al, viscous dislocation glide associated with solute drag is the rate controlling mechanism with an n value near 3 while for an n value near 5, creep deformation is governed by the climb of dislocations breaking away from the solute atmosphere. It was also reported that at high stresses a high stress exponent (n=11) was observed and that this may be caused by the interaction between dislocations and precipitates[24].

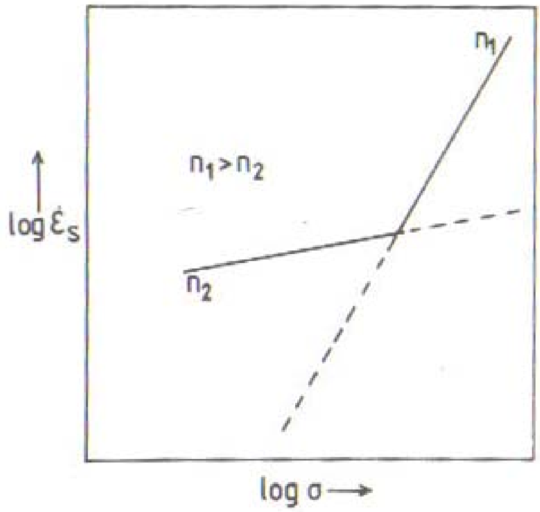

Fig.9 Variation of the secondary creep rate with stress when two independent processes contribute to the overall creep rate[5]

Fig. 9 shows the typical Norton plot for a metal when two independent processes with the stress exponents n_1 and n_2 ($n_1>n_2$) contribute simultaneously to the overall creep rate. It can be seen from the figure, that only at the stress level at which the non-parallel $\log \dot{\varepsilon}_s / \log \sigma$ relationships intersect the two processes contribute equally to the overall creep rate. At higher stress levels, the creep rate is determined by the deformation process with the larger n value, while at lower stress, the contribution made by the process with the larger n value decreases rapidly with decreasing stress. Thus the overall creep rate is governed by the process having the lower n value.

It was reported by Kimura et al. that according to the change of rupture time with stress, the controlling factor for creep resistance can be divided into three regimes, which is shown in **Fig. 10**[25]. Clearly, the way a metal resists creep in the plastic and the elastic regime should be different. In the plastic regime, the creep resistance is believed to be controlled by tensile/yield strength while in the elastic regime, the controlling factor was thought to be microstructural stability and the strength of the matrix. Usually, for industrial application, the stress for creep tests is in most cases chosen to be smaller than the yield stress of the material.

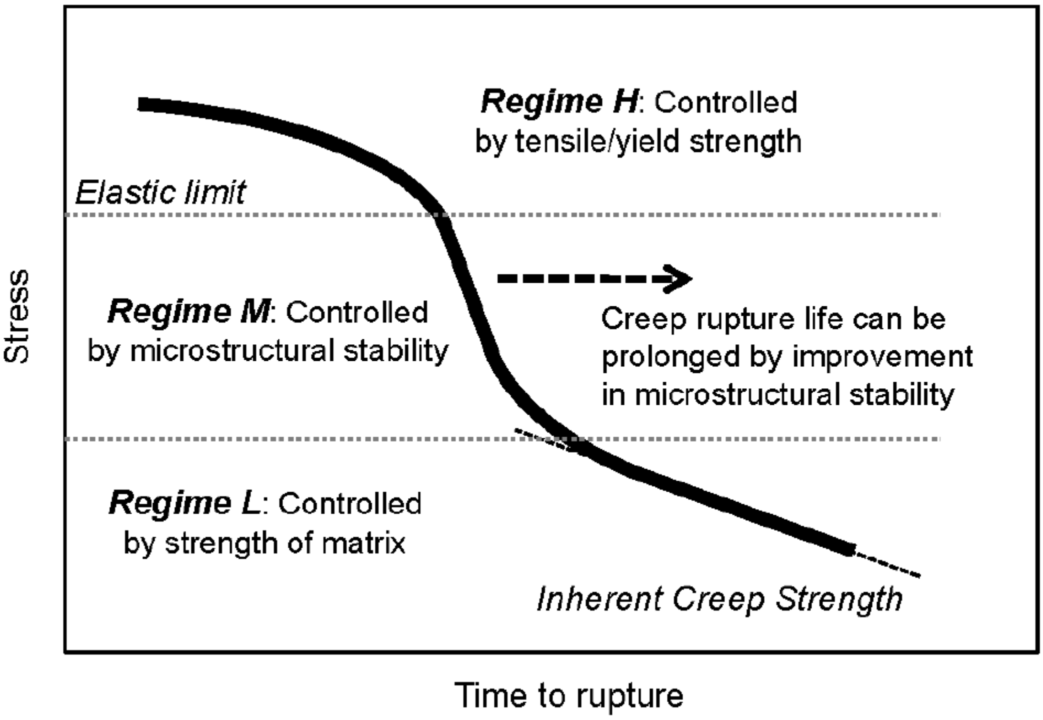

Fig. 10 Stress regimes and proposed corresponding materials' properties controlling creep strength according to [25]

2.3.2 Stress relaxation test

As conventional creep tests require many specimens to determine creep rates at different stress levels and the testing time is usually very long (up to several years), stress relaxation testing (SRT) can be a short cut for determining "minimum creep rates" at various stress levels in a single experiment. For life assessment of operating components, creep strength and fracture resistance are two important values. Since an enormous amount of data can be generated in a short time from the SRT, creep strength can be evaluated based on a high precision short time stress relaxation test[26]. However, there are also certain limitations of SRTesing, which are listed below:

1. Precise life assessment is not possible because SRT can not account for long-term microstructural changes
2. It only works with good “extrapolation” accuracy if secondary creep is the life-limiting stage

Nevertheless, despite of these limitations, SRT is a good tool for material development.

Although stress relaxation and creep are technically different, the net effect is the same, in that both mechanisms lead to the eventual exhaustion of a component’s ductility. Differences between creep rates measured in conventional creep testing and the plastic strain rates measured during stress relaxation tests can be caused by recovery during the relaxation phase and the precision of the Young’s modulus measurement, that is essential for data evaluation from SRT[27].

Stress relaxation tests are performed by applying a finite amount of strain ε_0 to a specimen and maintaining it constant while the stress σ drops with time. The principle of this testing method is assumed to be due to the conversion of the elastic strain ε_e in the specimen to the inelastic strain ε_p. Since the total strain $\varepsilon_0 = \varepsilon_e + \varepsilon_p$ is constant after the beginning of the stress relaxation, $d\varepsilon_0/dt = 0$ and for this reason $d\varepsilon_p/dt$ is given by:

$$d\varepsilon_p/dt = -d\varepsilon_e/dt = -d(\sigma/E)/dt \qquad \textbf{Equation 9}$$

Where E is the Young’s modulus and σ is the “remaining stress” at time t[27].

It is reported that for the titanium-based alloy Ti-6Al-2Sn-4Zr-6Mo, with increasing constant initial strain, the strain rate dependence of the stress exponent n* decreases, approaching the stress exponent value n typical for pure dislocation mobility induced viscous flow in many titanium alloys[28]. That means, with higher constant initial strain the strain rate deduced from the SRT would be more close to the actual creep test results.

For the actual execution of the experiment, many different testing procedures were adopted for the stress relaxation test to make the testing results more accurate. It was reported by Wada[2] that slight creep before stress relaxation can reduce scatter and corresponds better to the results measured in the conventional creep method. In other words: SRT has to be started from the secondary stage of creep.

3. Experimental

3.1 Overview of experiments

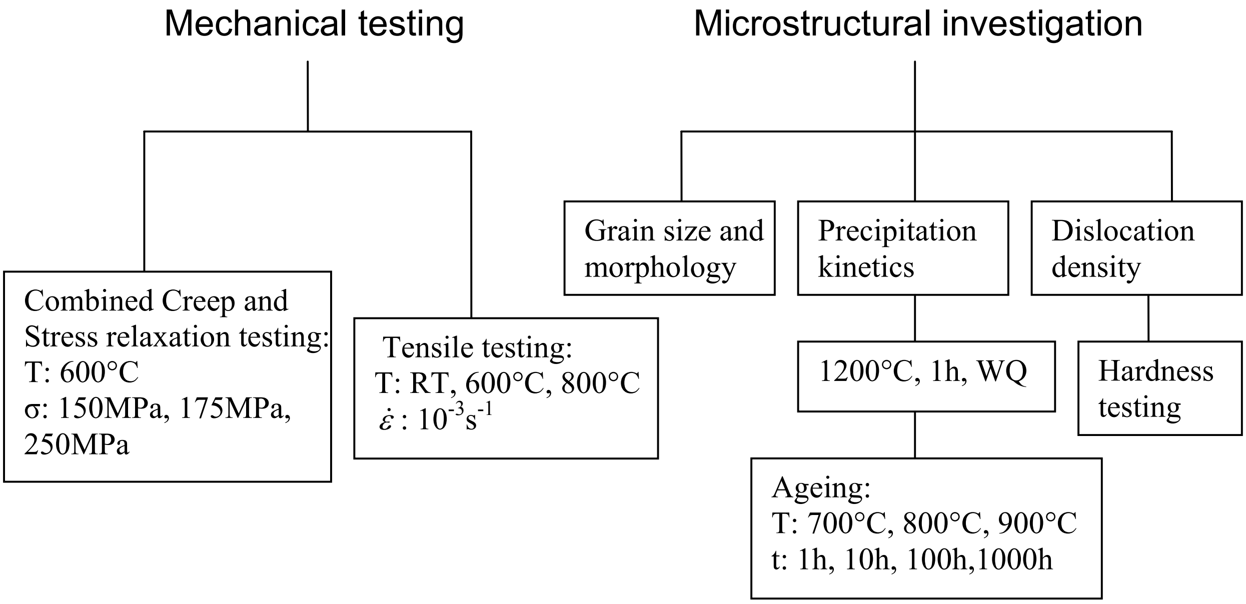

Fig.11 Plan of the experiments

3.2 Testing of mechanical properties

3.2.1 Specimen dimensions

Because of an imminent scarcity of 16mm slab materials from the laboratory melts 2mm sheet materials from the same melts have been selected for mechanical testing. For the half-commercial melt 2mm-sheets were chosen to make the results directly comparable even if there was no shortage of 12mm slab material. Specimens from the 2mm sheet materials were laser-cut into the dog-bone shape given in **Fig.12** (86mm×25mm×2mm with a gauge length of 10mm).

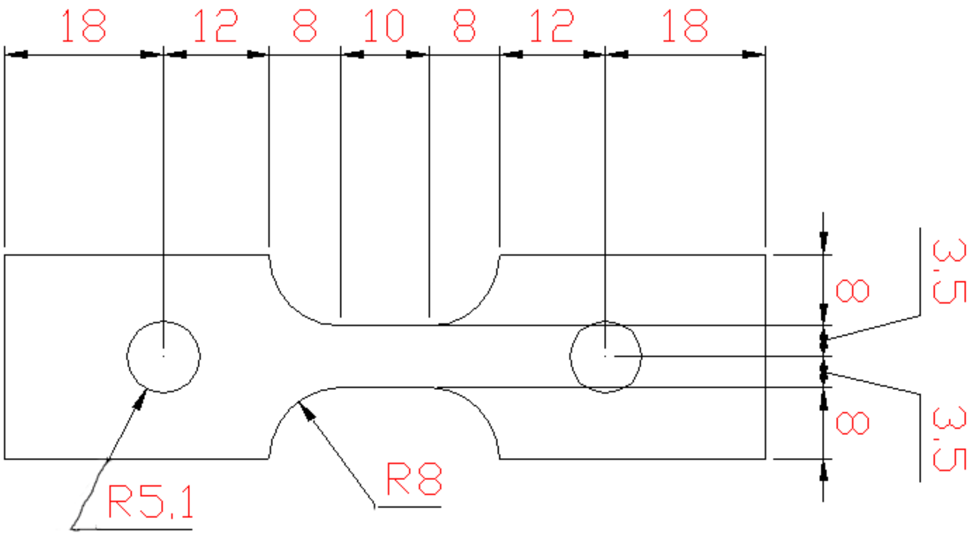

Fig.12 Dog bone specimen for mechanical testing of sheet materials

3.2.2 Testing procedure

Tensile tests:

Tensile tests were conducted at room temperature, 600°C and 800°C. The strain rate for all the tests was $10^{-3}s^{-1}$. An Instron Type 1381 testing machine was used in the tensile experiments.

During the experiments, the specimens were heated to the testing temperature by resistance heating with a heating rate of about 10°C/min. The temperature of the specimen was monitored by a Pt/RhPt thermocouple attached to one end of the specimen and the temperature fluctuation was controlled within ± 1°C during the tests. The extensometer fitting consisted of a rod and tube assembly which transfers the extension of the specimens to two linear variable differential transformers (LVDT's) mounted outside of the furnace. It is important to notice that the extensometer could not be attached directly to the specimen because of its sheet configuration. The implications of this fact will be explained in section 3.2.3.

Fig.13 Overview of the testing set-up

Stress relaxation test:

The purpose of the stress relaxation tests was to obtain as much information as possible concerning the strain rate evolution with changing stress. For each experiment, two stages with different initial stress levels were applied with both creep and relaxation period. That means, in each stage, the specimen was first loaded to the desired stress level and then crept at constant stress until the secondary creep stage was reached. During this period, the secondary creep rate at constant stress was obtained (similar to conventional creep testing). After that, the strain was held constant and the stress relaxation part was started till almost constant stress. Then the second stage was started with loading up once again to the second desired stress level repeating the described combined creep and SRT test cycle. In that way, a wide range of stress levels were covered and corresponding creep rates could be obtained. **Fig.14** depicts stress vs. time and strain vs. time visualizations of the testing procedure.

All the stress relaxation tests were also conducted in an Instron Univeralprüfmaschine 1381. During the experiment, the specimens were heated up to the objective temperature in the concealed machine furnace by resistance heating. The temperature increase rate was about 10 K/min. Before the experiments started, the total time for the heating and equalizing period is 4 hours. Loading rate was about 5MPa/s.

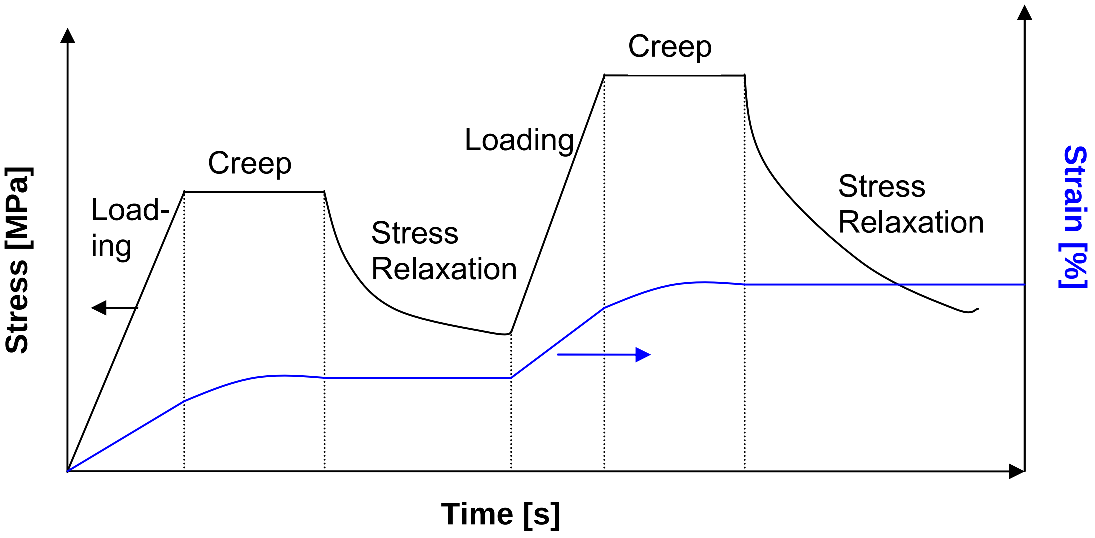

Fig.14 Ideal stress-time, strain-time curves expected in the stress relaxation test

3.2.3 Machine correction

Fig.15 displays the principle of the strain measurement method utilized in the stress relaxation tests. Because of the sheet configuration of the sample material, the strain measurement could not be conducted directly at the specimen gauge. Instead the strain of the whole specimen ε_{SH} together with the strain of part of the machine ε_t was measured, which can be expressed in the following equation:

$$\varepsilon_t = \varepsilon_{SH} + \varepsilon_m \text{ (}\varepsilon_m \text{ is the machine strain)} \qquad \textbf{Equation 10}$$

To get the specimen strain from the relaxation test the recorded raw data has to be corrected for machine strain. For this purpose the machine strain has been recorded utilizing a couple of extraordinary stiff IN 617 calibration samples.

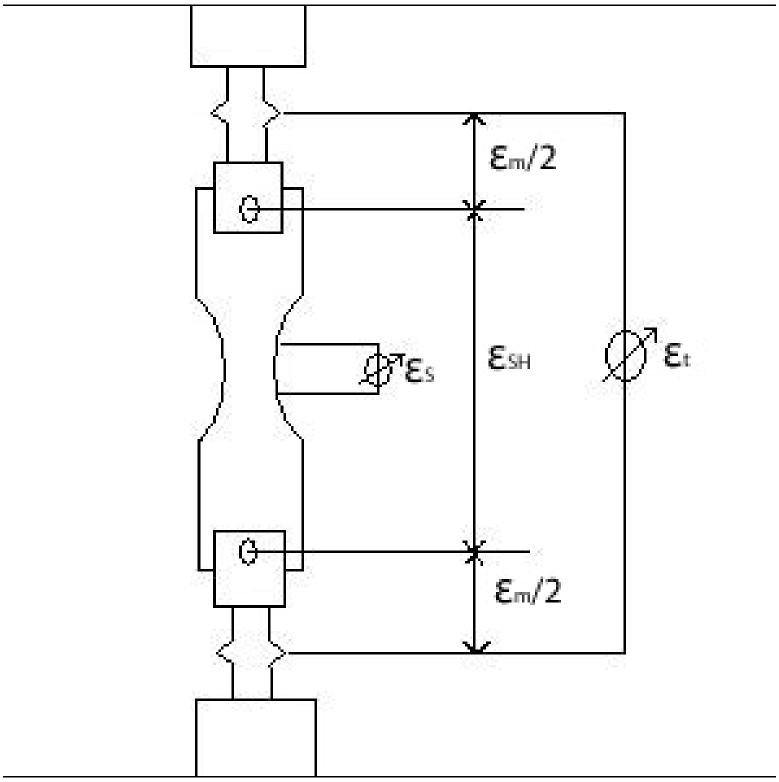

Fig.15 Strain measurement in the stress relaxation test

The change of the machine strain with the corresponding stress is shown in **Fig.16**. Because of the scatter of the raw data, a 4th order polynomial fit with an accuracy of at least 99% was conducted. With the help of equation $Y = 3.22{\cdot}10^{-10}{\cdot}x^4 - 1.78{\cdot}10^{-7}{\cdot}x^3 - 3.8{\cdot}10^{-5}{\cdot}x^2 + 6.83{\cdot}10^{-3}{\cdot}x - 1.7{\cdot}10^{-2}$, any machine strain (Y) within the stress range can be deduced by entering the stress value (x). During the stress relaxation test, the total strain ε_t was held constant by the machine, but with the decrease of the load, machine strain ε_m is also decreasing. According to **Equation 10** that means specimen strain ε_{SH} has to increase to maintain the constant total strain ε_t.

Therefore, during the data analysis of the testing results, the creep rate of the specimens at certain stress level comprises of two parts: The first part is the strain rate in which the elastic strain transfers to plastic strain, which can be deduced from the change of the stress with time and the Young's modulus; the other part is the strain rate which is caused by the decreasing machine strain with decreasing load. An example of the calculation procedure will be specifically explained in chapter 4.4.2.1.

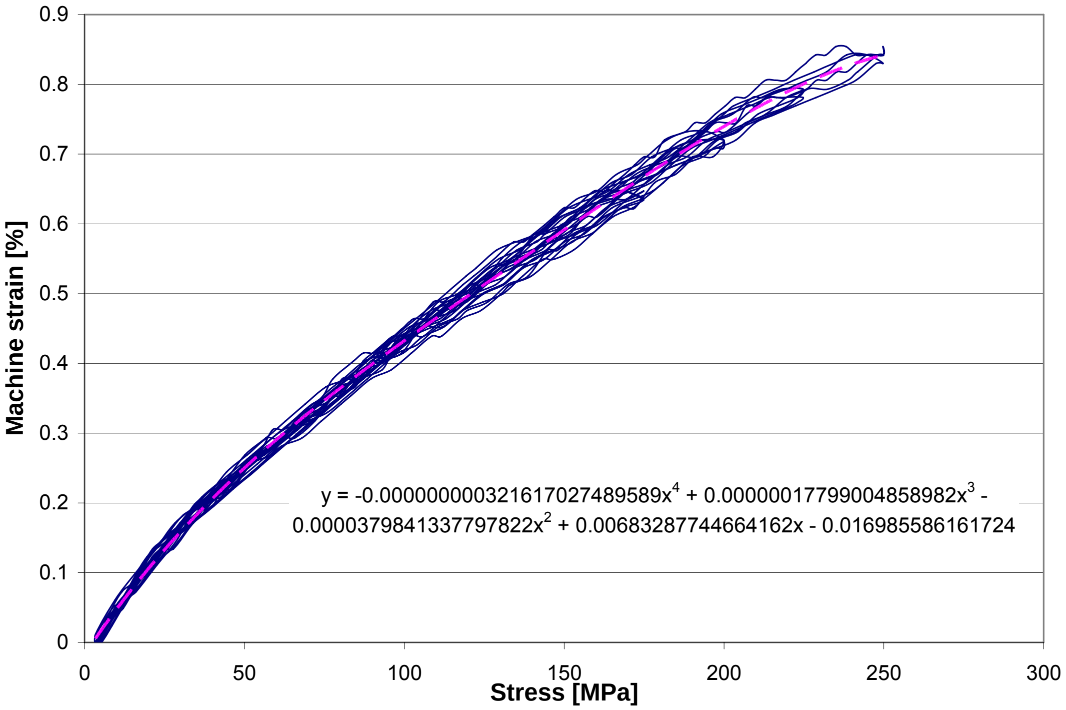

Fig.16 Evolution of machine strain with stress

3.3 Microstructural investigation

3.3.1 Annealing experiments

Cubes of 5mm lateral length were cut from the slab materials for annealing experiments. In order to prevent oxidation and evaporation of alloying elements (like La, Cr, Mn…) during the heat treatment experiments, the specimens were sealed in silica glass capsules filled with an inert cover gas (Ar 4vol.-%. H_2).

Investigation of the precipitation kinetics was conducted by solution treatment at 1200°C for 1h followed by ageing at different temperatures (700°C, 800°C, 900°C) for different times (1h, 10h, 100h, 1000h). The purpose of solution treatment is to solve all the existing precipitates and to get a “standardised” microstructure concerning grain morphology, size and precipitates for all the materials under investigation. The following table shows the course of the experiments:

Tab.1 Overview of the annealing experiments

Solution treatment: 1200°C, 1h, Water Quenching KSX: 007-018; KUB: 007-019; MGQ: 007-019			
Ageing	700°C	800°C	900°C
1h	KSX;KUB;MGQ:007	KSX;KUB;MGQ:011	KSX;KUB;MGQ:015
10h	KSX;KUB;MGQ:008	KSX;KUB;MGQ:012	KSX;KUB;MGQ:016
100h (4days4h)	KSX;KUB;MGQ:009	KSX;KUB;MGQ:013	KSX;KUB;MGQ:017
1000h (41days16h)	KSX;KUB;MGQ:010	KSX;KUB;MGQ:014	KSX;KUB;MGQ:018

3.3.2 Sample preparation

For microstructural investigation, all the as-received specimens were first hot mounted at 150°C, 200Pa in a hot-mounting machine. The specimens were then grinded using SiC paper starting from P120 and going down to P1200. After grinding, the specimens were polished using diamond particles from 6μm to 1μm size in water-based solution. The final polishing was done by vibration polishing in dilute KOH solution for 5 hours.

3.3.3 Hardness testing

All the hardness tests were conducted using a Fischer Type Indentation machine. In order to obtain data for quantification of dislocation density, different indentation force levels were chosen as follows: 10 mN, 20 mN, 50 mN, 70 mN, 300 mN, 500 mN, 700 mN. At each indentation point, HV (Vickers' hardness), h_{max} (maximum depth of each indentation) and E (Young's modulus) were measured. For the 10mN force level, 30 points were measured and the average value was calculated. With the increase of the force level, the scatter of the data decreases, therefore 20 points were taken for 20mN to 70mN while for force levels from 300mN to 700mN, only 10 points were measured. As has been discussed in the literature review part, the squared value of the hardness against the inverse value of the maximum depth was plotted and the intrinsic hardness can be deduced from the curve equation. In this way, the dislocation density of the material was calculated referring to the Nix-Gao-model.

3.4 Production parameters of the materials

In order to identify the detrimental factor that results in the poor creep performance of MGQ (MDO), two different laboratory melts KUB (KUA) and KSX (KSY) were selected as the basis for comparison. **Diag.1** shows the three melts and their corresponding slab and sheet materials.

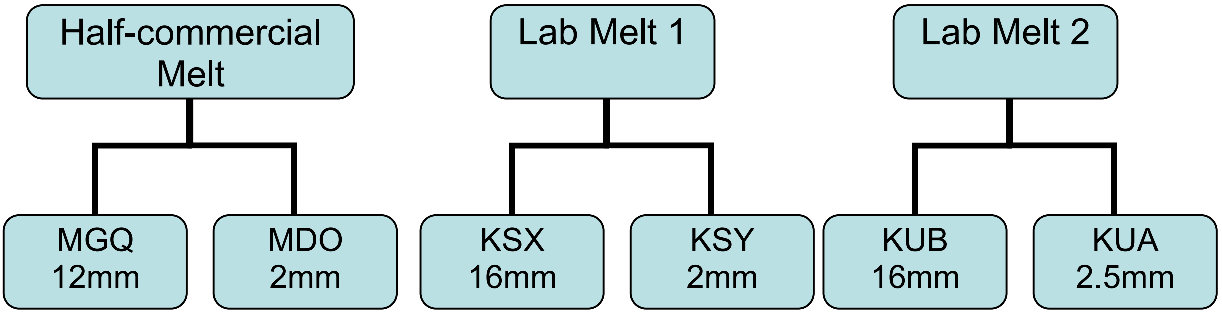

Diag.1 Illustration of the investigated materials and their corresponding melts

Tab.2 shows the chemical composition of the three melts. Carbon and nitrogen content are higher in the half-commercial melt (MGQ, MDO) and laboratory melt 1 (KSX, KUA) than in laboratory melt 2 (KUB, KUA). The impurity content (C, N, P, Al…) is higher in the half-commercial melt than in the two lab melts. The content of La is much lower in laboratory melt 1 (KSX, KSY) than in the other two melts.

Because of differing production ways, the processing procedures were different for laboratory and half-commercial melts. **Tab.3 and Tab.4** contain the production parameters for each material. The production procedures were the same for both sheet and slab laboratory materials. However, for the half-commercial materials, the 2mm sheet material was – in contrast to the slab material – hot and cold rolled, plus its solution treatment differed from the 12mm slab material (**Tab.4**).

Tab.2 Chemical composition of the steels used in the present study

Element in Masse%	MGQ (MDO)	KSX (KSY)	KUB (KUA)
C	0.007	0.003	<0.002
S	<0.002	0.003	<0.002
N	0.015	0.014	0.007
Cr	22.93	22.56	22.32
Ni	0.3	< 0.01	<0.01
Mn	0.43	0.45	0.43
Si	0.21	0.25	0.24
Si_W		0.24	0.27
Mo	0.02	0.01	0.01
Ti	0.07	0.04	0.06
Ti_W		0.039	0.065
Nb	0.51	0.57	0.48
Cu	0.02	0.01	<0.01
Fe	73,26R	74.449 R	74.469 R
P	0.014	0.0040	0.003
Al	0.02	0.003	0.009
Al_W		0.002	0.005
Mg	<0.01	< 0.01	<0.01
Mg_W		0.0002	0.0001
Ca_W		0.0003	<0.0002
La	0.08	<0.01	0.06
La_W		0.010	0.093
W	1.94	1.75	2.02
O		0.008	0.008

Tab.3 Processing parameters of the three slab materials

Slab – batch ID	MGQ	KSX	KUB
Heat treatment before hot rolling	Unknown	1080°C, 2h	1080°C, 2h
Hot rolling	Unknown	980°C, air cooling	980°C, air cooling
Solution treatment	1075°C, 22 min air cooling	no	no

Tab.4 Processing parameters of the three sheet materials

Sheet – batch ID	MDO	KSY	KUA
Heat treatment before hot rolling	Unknown	1080°C, 2h	1080°C, 2h
Hot rolling	Unknown	980°C, air cooling	980°C, air cooling
Cold rolling	Yes	No	No
Solution treatment	1050°C, 3.4min Jet cooling	No	no

4. Results and discussion

4.1 Creep properties of the slab materials

In former creep experiments of the slab materials, turned specimens (Ø: 6.4mm, gauge length: 30mm) were tested in the temperature range from 600°C to 800°C at different stress levels. Compared to the laboratory batches KSX and KUB the half-commercial batch MGQ failed quickly in the 600°C creep tests. However, it behaved relatively stable in the 800°C creep tests, rather comparable to the laboratory batches, as can be seen from the results in **Tab.5**.

Considering the stress levels of the creep tests, dislocation dominated processes should have been prevailing at 600°C, while the creep mechanism at 800°C, 10MPa should have been diffusion dominated. The rapid failure of annealed MGQ at 600°C might indicate that precipitates dissolution due to solution treatment of the half-commercial batch might not be the only reason for the degraded creep strength. Considering all factors stated above (**Tab.3**), reduced dislocation density of MGQ because of solution treatment might be another possible reason for the unexpectedly quick failure at 600°C. Based on these results of former creep experiments, the main issue of this thesis is to find out if the change in dislocation density caused by heat treatment was the major factor for the degraded mechanical behavior of the half-commercial alloy at 600°C. Furthermore, this idea is endorsed by the fact, that creep of MGQ at 800°C and low stress (10MPa) – where creep is diffusion dominated and dislocation density has minor influence – seems to be quite similar to the lab melts.

Tab.5 Creep testing results for the three melts (turned specimens) at different temperature and stress levels

	Running time	Strain	State	Processing
600°C, 120MPa				
KSX	19014	0.15	Still running	Hot rolled
KUB	19001	0.42	Still running	Hot rolled
MGQ	93	53	Failure	Solution treated
MGQ	28	61.5	Failure	Annealed: 700°C, 10h
600°C, 145MPa				
KSX	7545	9.21	Failure	Hot rolled
KUB	860	18.82	Failure	Hot rolled
MGQ	92	49	Failure	Solution treated
800°C, 10MPa				
KSX	14849	28.016	Failure	Hot rolled
KUB	12709	45	Failure	Hot rolled
MGQ	4926	3.08	Still running	Solution treated

Detailed examination of the creep behavior of the two laboratory batches shows that although KSX and KUB are superior to MGQ, KSX always exhibits better creep strength than KUB, as can be seen from **Fig.17**. So another task in microstructural investigation is to find out possible reasons for this difference in creep resistance.

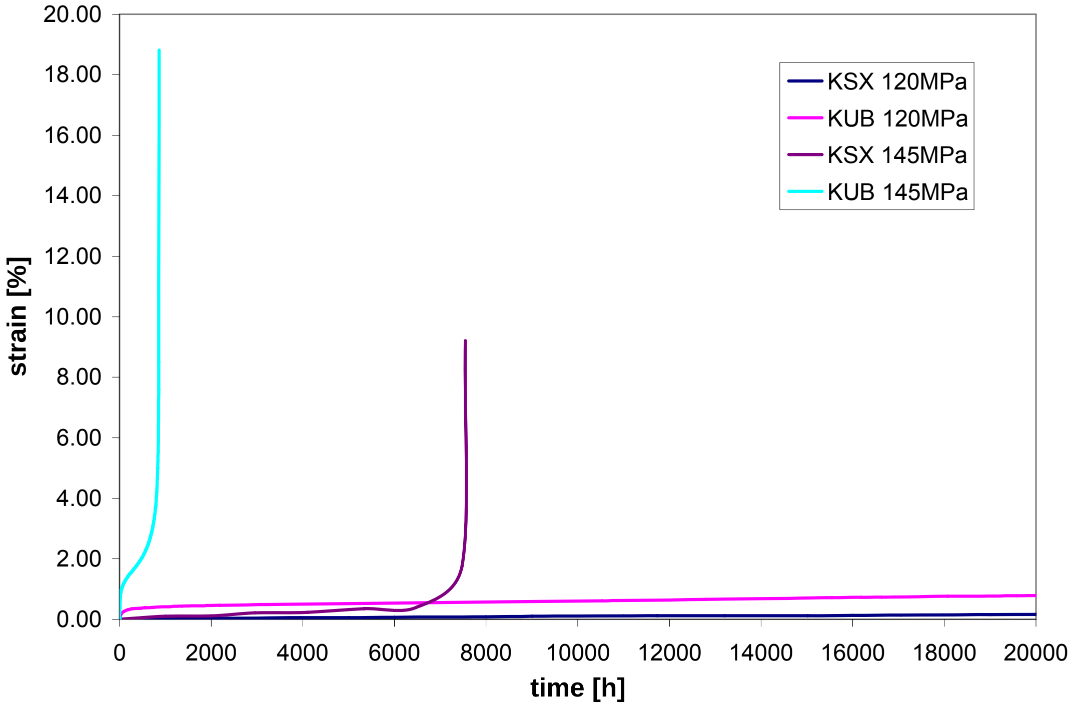

Fig.17 Creep curves of turned specimens from slab materials KSX and KUB at 600°C

4.2 Microstructure

According to the chemical composition and processing parameters of the three batches, the reasons that might have caused the degradation of creep strength of MGQ may be the following:

1. Different grain size and grain morphology caused by different production processes.
2. Differences in chemical composition might have caused different precipitation kinetics, which would affect the stability of the materials during long term creep.
3. Loss of initial strength because of reduction of dislocation density during the commercial production process (extra solution treatment of the commercial material MGQ).

As discussed previously, the third point was supposed to be the main reason. However, more evidence and experimental results were needed to prove that. The objective of the microstructural investigation was to find out whether there were differences regarding the three given aspects and how strongly these differences would influence the material’s high temperature mechanical behavior.

4.2.1 Grain size and morphology

During investigation of the grain morphology of the six materials (both slab and sheet specimens for the three melts), it was found that the slab material KSX has an inhomogeneous grain morphology throughout the whole cross section, which is shown clearly in **Fig.18**. The reason for this might be the production process of the laboratory melts. Temperature fluctuation in the process may have caused inhomogeneous deformation of the material.

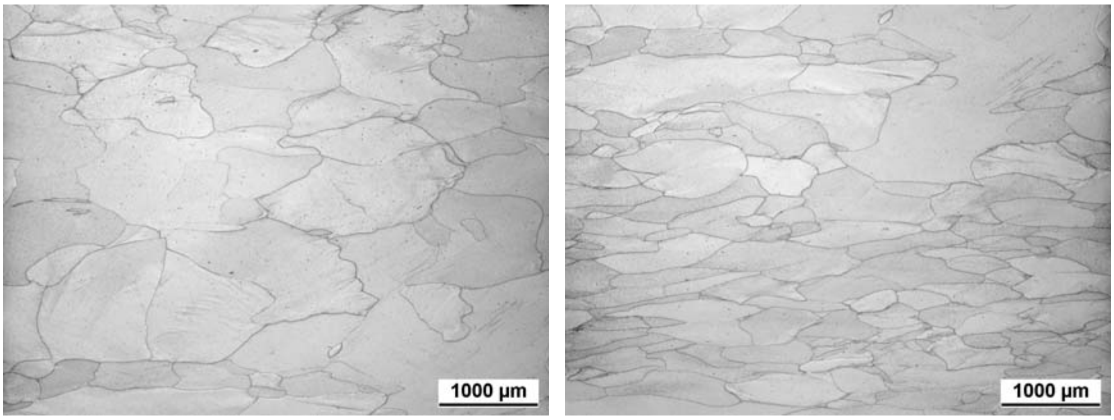

Fig.18 Grain morphology of KSX at different locations of the cross section

Besides KSX, all the other batches show homogeneous grain structures throughout the whole cross section. **Fig.19** shows the grain size and morphology of both slab and sheet material for the six material batches in the as-received state.

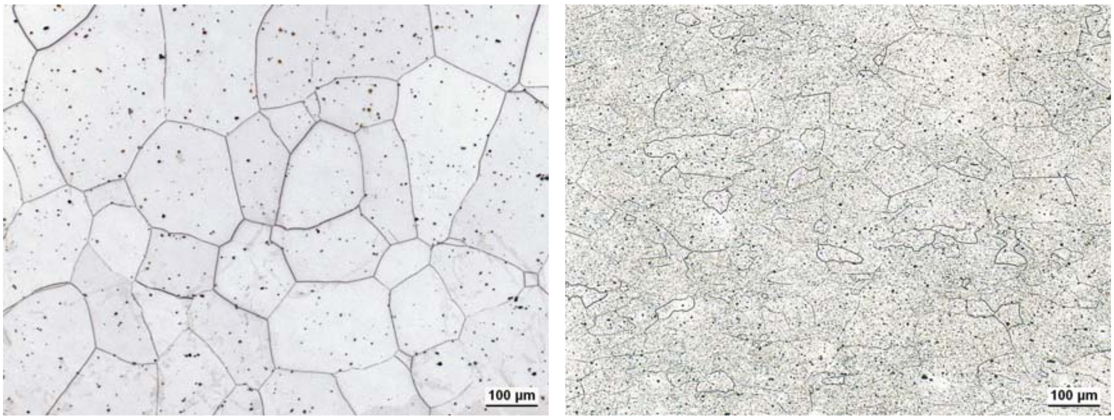

(a) MGQ (12mm slab) (b) MDO (2mm sheet)

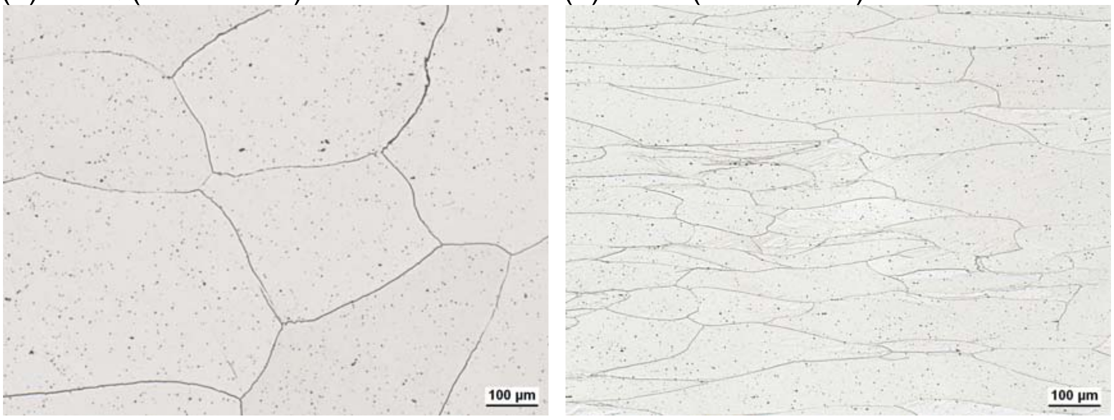

(c) KUB (16mm slab) (d) KUA (2.5mm sheet)

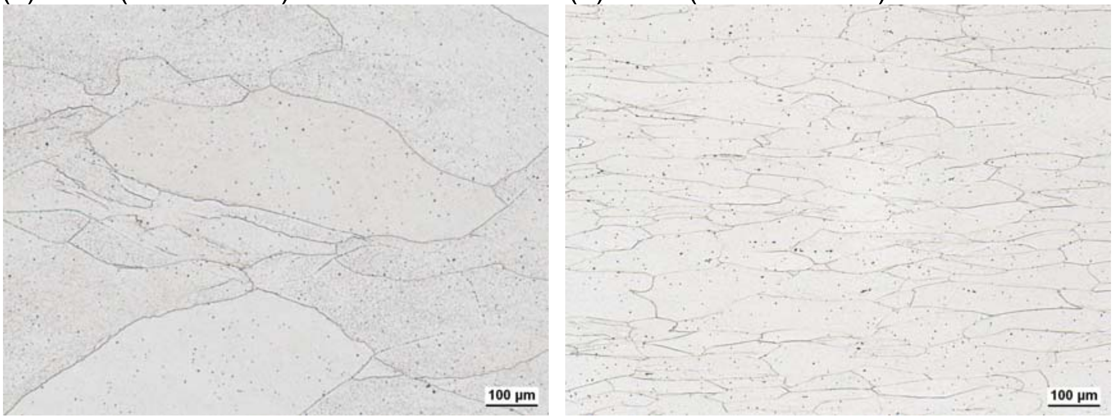

(e) KSX (16mm slab) (f) KSY (2mm sheet)

Fig.19 Grain morphology of the six materials

With respect to the laboratory slab materials, KUB shows a more integral grain structure in comparison to KSX in spite of nominally same material processing procedures. As stated before, KSX might have been produced with imprecise temperature control during production, while for KUB the temperature seems to have been high and homogeneous enough for a complete dynamic recrystallization to occur during the hot-rolling process. Comparison between the sheet specimens and the slab specimens shows that the sheet specimens exhibit more deformed grain structures than that of the slab specimens. That is mainly because of the higher extent of deformation during the hot rolling from ingot to 2mm sheets.

For the half-commercial materials MGQ and MDO, both show typical solution treated grain morphology. However, recrystallization seems to be more advanced in MGQ than in MDO. This could be induced by different solution treatment conditions and the different dimensions of the materials during heat treatment.

4.2.2 Precipitation investigation

According to SEM results, typical precipitates that appear in this kind of materials are: Laves-phase particles, LaO, MX particles and σ-phase precipitates. In the following the kinetics of precipitation and the distribution of precipitates will be discussed.

4.2.2.1 Precipitation kinetics and distribution of Laves-phase particles

Laves-phase precipitates are believed to be the main strengthening precipitates in this brand new creep-resistant alloy. They usually form at high temperature and are relatively stable (up to ~980°C)[29]. Because of different processing procedures, even slab and sheet specimens from the same melt may exhibit different precipitates distribution in the as-received state. **Fig.20** shows the distribution of laves-phase precipitates of the slab materials KSX, KUB and MGQ and of the corresponding sheet materials KSY, KUA and MDO.

KSX (KSY) and KUB (KUA) were in the hot-rolled state, while MGQ (MDO) was in the solution-treated state before creep testing. For the half-commercial batch, because of industrial production requirement, the sheet material MDO had an extra cold rolling procedure and the heat treatment parameters were different from those of the slab material MGQ (**Tab.3)**. These factors obviously caused widely different precipitate distributions in the two materials: In MGQ, most laves-phase precipitates were dissolved because of the solution treatment lasting for 22 minutes, while in MDO laves-phase precipitates distributed rather homogeneously all over the matrix. These differences could only be caused by differing production processes because the materials were from the same melt. Precipitation kinetics are mainly influenced by chemical composition and thus both batches should be comparable.

For the laboratory melts, because of the same processing procedures, sheet specimens and slab specimens from the same batch should show similar precipitation behavior, which is the case for the laboratory batches KUB and KUA. However, from **Fig.20 (a)** and **(d)** it is clear that even though slab material KSX and sheet material KSY are from the same melt, laves-phase shows different precipitation behavior. Small laves-phase particles distribute homogeneously inside the grains of KSX; while the matrix of the KSY is relatively clean from laves-phase precipitates.

The same phenomenon was observed in comparing the two laboratory slab specimens. It was found that although similar chemical composition and processing procedures were applied, the precipitation behavior of Laves-phase particles is still different, as is shown in **Fig.20 (a)** and **(b)**. The reason for this might be:

1. Small chemical composition differences (inhomogeniety) leading to different precipitation kinetics;
2. Undefined processing differences in the production process.

Considering the difference between slab material KSX and sheet specimen KSY, it is believed that this was caused by temperature fluctuation during production of the KSX material. Nevertheless, more information concerning the microstructure of these materials is needed to confirm this uncommon precipitation behavior.

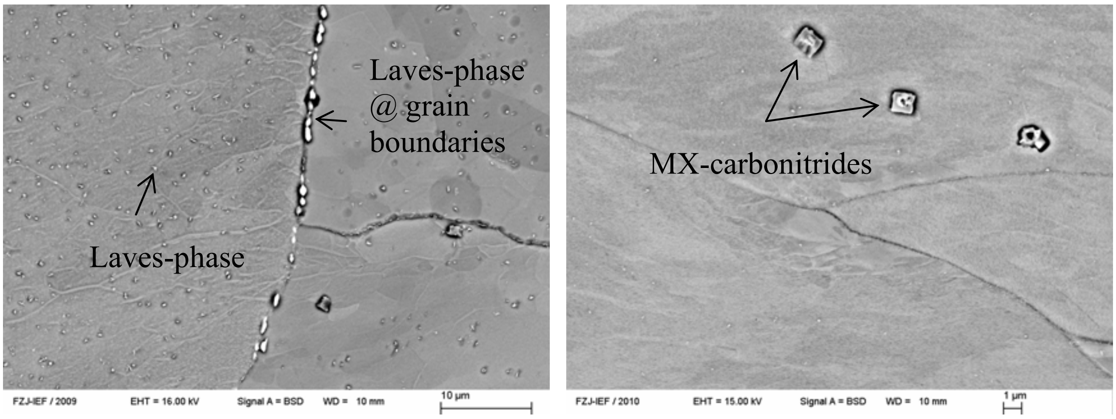

(a) KSX (16mm slab) (d) KSY (2mm sheet)

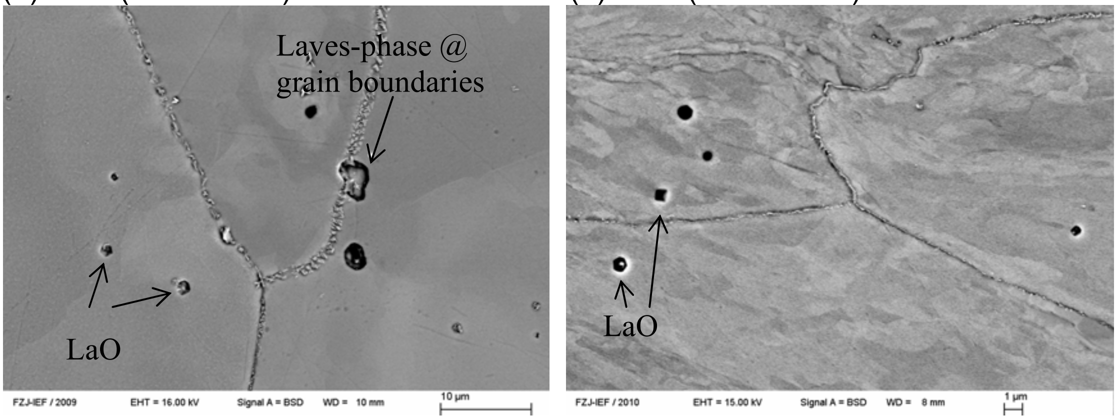

(b) KUB (16mm slab) (e) KUA (2.5mm sheet)

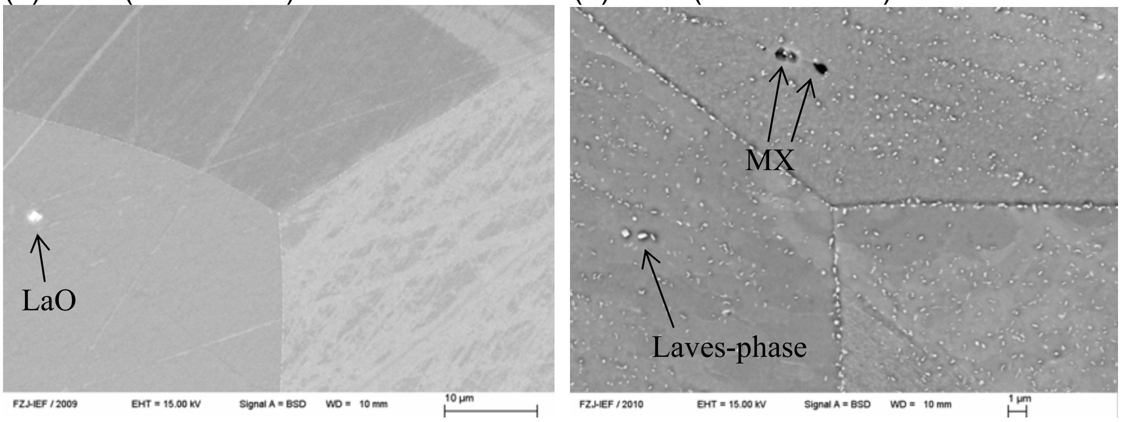

(c) MGQ (12mm slab) (f) MDO (2mm sheet)

Fig.20 Laves-phase distribution in 22mm slab material (a) KSX; (b) KUB; (c) MGQ; (d) KSY; (e) KUA; (f) MDO

To find out the exact reason for the different precipitation behavior, further microstructural investigation was conducted. To understand the precipitation kinetics of the three materials, annealing experiments with different temperatures and times were done with slab materials. The temperature range of the annealing experiments was from 700°C to 900°C. Annealing experiments at 700°C give the results closest to power plant application (600°C°~650°C). Annealing at higher temperatures would render more information concerning the sensitivity of the laves-phase precipitates to temperature as well as its applicability at higher temperatures. As stated before, the creep behavior of the half-commercial batch MGQ at 800°C was good, relatively comparable to the laboratory melts. Therefore, comparison of the precipitation kinetics at higher temperatures may also render information concerning the mechanical property change of the half-commercial batch.

Fig.21 shows the precipitate distributions of the slab materials after 10 hours of annealing at 700°C. Clearly, the two laboratory specimens KUB and KSX show roughly comparable precipitation kinetics. This is another hint that unexpected temperature fluctuation in the production process of KSX might have caused its distinctive precipitation behavior. For MGQ laves-phase precipitation unexpectedly exhibits great inhomogeneity compared to that of the laboratory materials. The laves-phase precipitates distributed sparsely at some locations, while in other areas of the matrix they were as concentrated as they were in the two laboratory materials.

Nevertheless, despite of the inhomogeneous laves-phase precipitation of MGQ at the initial annealing stage, it homogenized with time. **Fig.22** shows the microstructure after 100 hours and 1000 hours of annealing at 700°C. With longer annealing time, the precipitates coarsened and homogenized all over the matrix. After 1000 hours of annealing, the laves-phase precipitates were almost as homogeneously distributed as those in the laboratory materials.

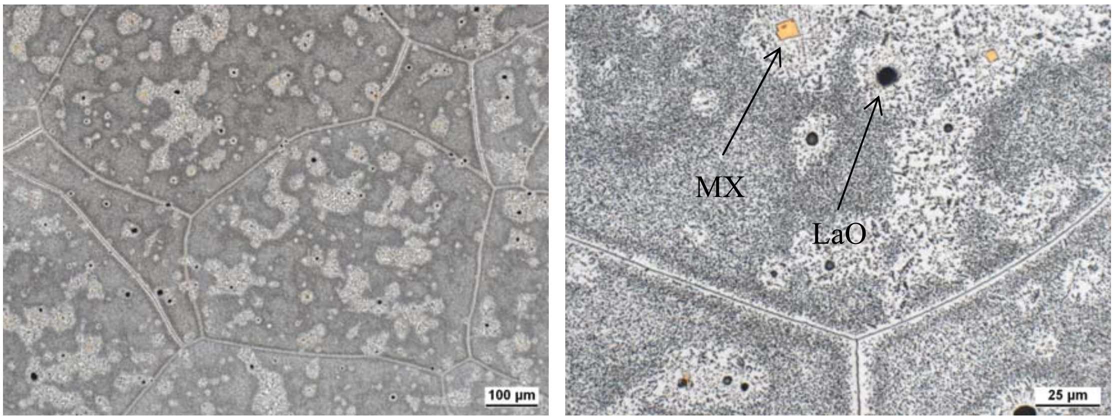

(a) MGQ008 (12mm slab) (b) MGQ008 (12mm slab)

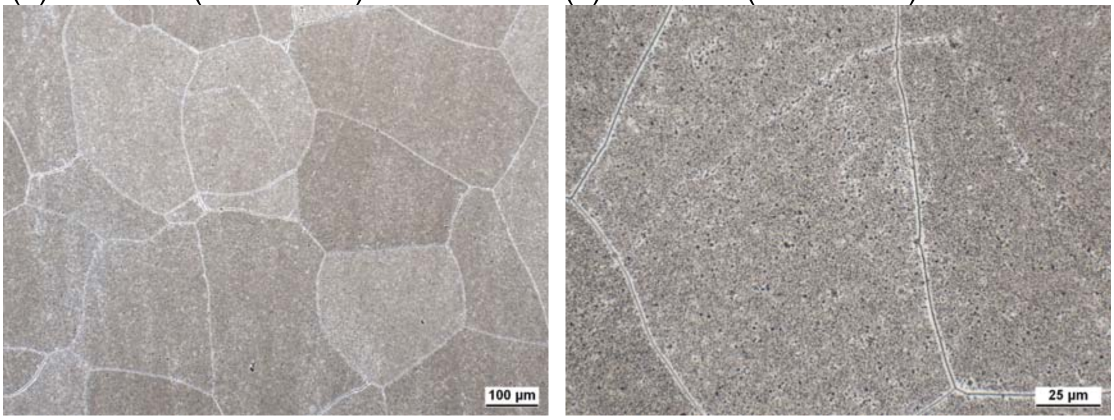

(c) KSX008 (16mm slab) (d) KSX008 (16mm slab)

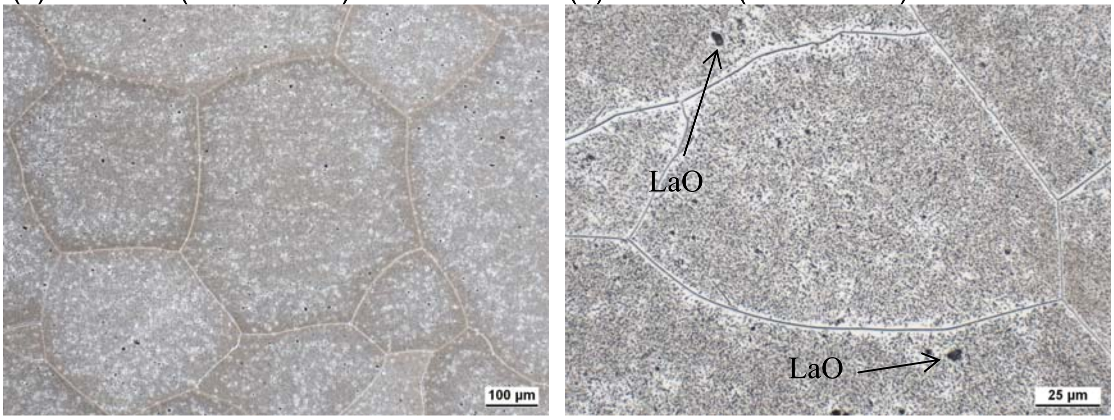

(e) KUB008 (16mm slab) (f) KUB008 (16mm slab)

Fig.21 Precipitate distribution of MGQ, KSX and KUB after 10 hours annealing at 700°C

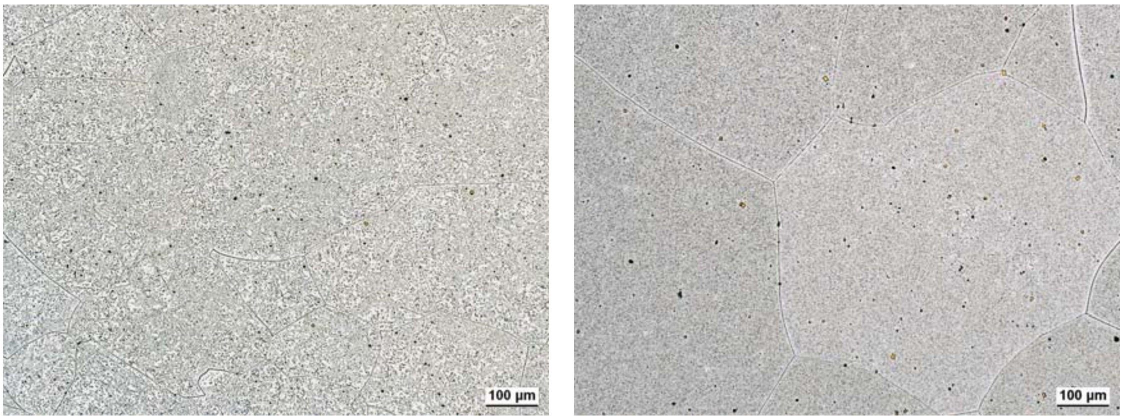

(a) MGQ009 (12mm slab) (b) MGQ010 (12mm slab)

Fig.22 Precipitate distribution of (a) MGQ009, annealed at 700°C, 100h; (b) MGQ010, annealed at 700°C, 1000h

For higher annealing temperature (800°C and 900°C), the homogeneity is improved. **Fig.23** shows the precipitate distribution after annealing at 800°C and 900°C for 10 hours. These findings suggest that diffusion can smooth out the inhomogeniety of laves-phase precipitation. This kind of diffusion-smoothed precipitation profile might also contribute to the fact that MGQ shows better creep performance at high temperature than that in the low temperature regime.

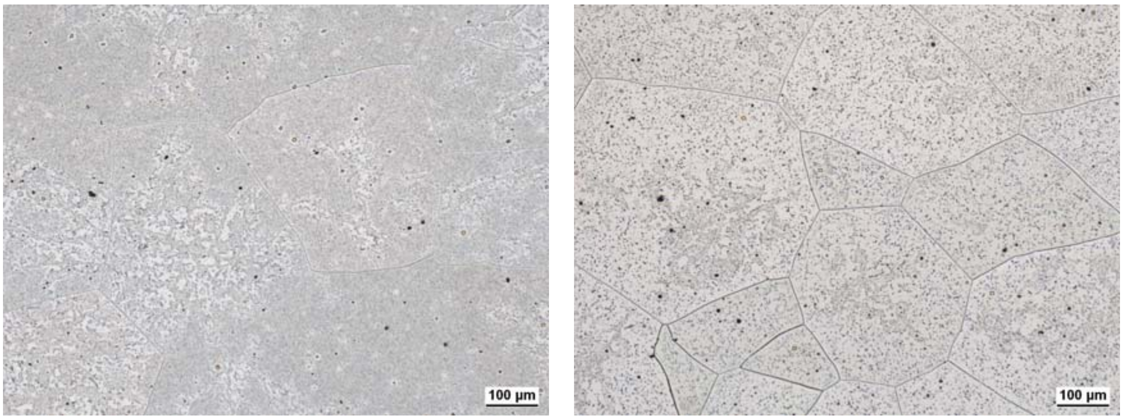

(a) MGQ012 (12mm slab) (b) MGQ016 (12mm slab)

Fig.23 Precipitate distribution of (a) MGQ012, annealed at 800°C, 10h; (b) MGQ016, annealed at 900°C, 10h

Based on the previously discussed results, the reasons for the differing precipitation behavior of the half-commercial material were suspected to be the following:

1. Lack of Nb and W in the matrix of the sparse-precipitate locations. Since these two elements are laves-phase forming elements, laves-phase precipitation would be delayed with a lack of these elements. The depletion of these elements might be caused by the high amounts of C and N in MGQ. Like it has been discussed in the literature review part Nb is an MX-particle forming element and has high affinity to C and N. Formation of MX-particles in MGQ might have reduced the amount of Nb in the surrounding matrix, thus reducing the reservoir for laves-phase precipitation.
2. Another suspect was based on the observation that most of the sparse-precipitate locations are places where other precipitates like MX-particles and LaO are located. On the contrary, in the laboratory materials KSX and KUB, the laves-phase precipitates around those MX and LaO precipitates are as concentrated as they are all over the matrix. It was thought that during the solution treatment of MGQ, most of the Nb and W were dissolved in the matrix because laves-phase dissolves at such high temperature. However, around those stable carbonitrides (which do not dissolve at the solution treatment temperature) the lattice was distorted. Considering the large atom size of Nb and W, most of them were expelled from the neighborhood of those precipitates. So instead of homogenizing the material, solution treatment actually caused “inhomogeneous” solid solution distribution in MGQ-material.

These theories are based on the limited information gathered up till now. To further prove the mechanism behind this phenomenon more experiments are needed.

4.2.2.2 Other precipitates found in Crofer 22H

Comparing the chemical composition of the three batches, the carbon and nitrogen contents of the batches MGQ (MDO) and KSX (KSY) were higher than that of KUB (KUA). Accordingly, during the precipitates investigation, lots of MX-particles were found in MGQ (MDO) and KSX (KSY). EDX measurement shows that these MX particles are

Ti and Nb-containing carbonitrides. **Fig.24** shows the typical morphology and chemical composition of these precipitates.

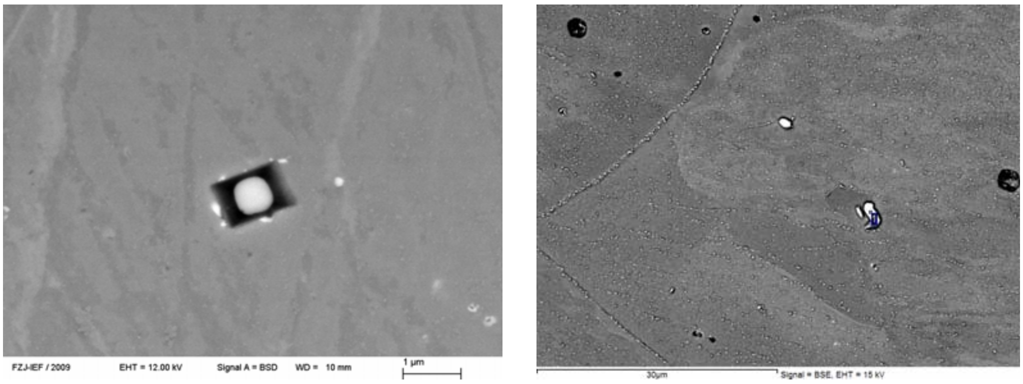

(a) Ti/Nb/N precipitate (b) Nb/C precipitate

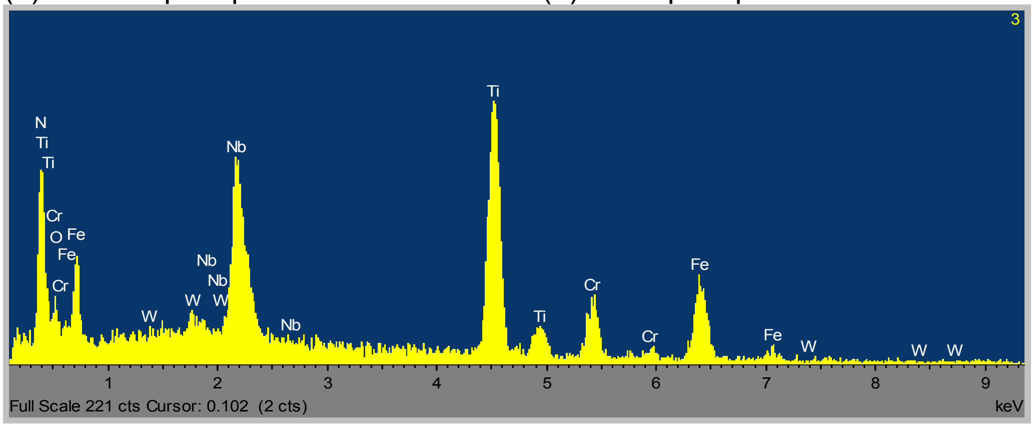

(c) Corresponding chemical composition of (a)

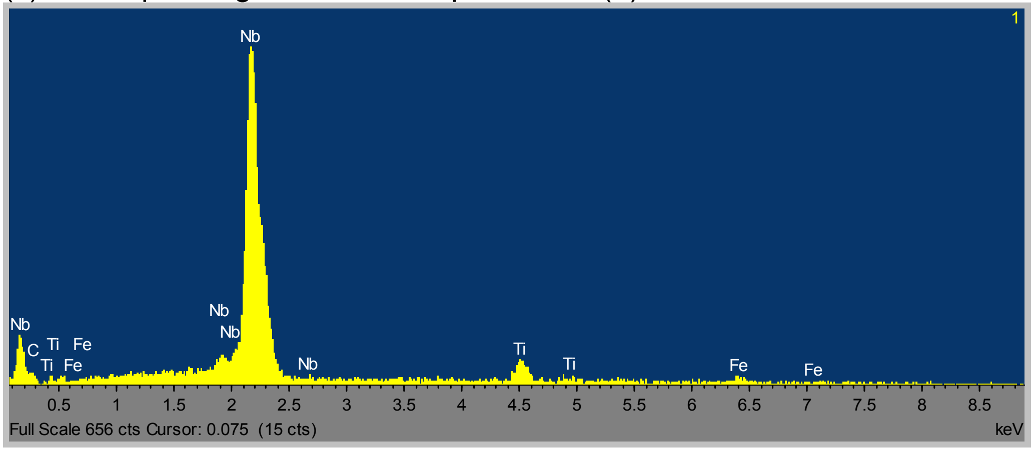

(d) Corresponding chemical composition of (b)

Fig.24 Typical morphology of carbonitrides and their chemical composition observed in KSX/MDO

These MX-carbonitrides are treated as the main strengthening precipitates in conventional martensitic ferritic steels. However, as discussed in the literature review part, these precipitates are very stable, even up to the melting point of the steel. Therefore they are very difficult to control during production. On the other hand, in the investigated materials, the amounts of these precipitates are relatively low. With the information gathered until now, it is believed that MX hardly contributes any strengthening effect to the material itself. On the other hand, as they can consume Nb, which is a very important element for both solid solution strengthening effect and for laves-phase precipitates strengthening, these MX carbonitrides may be considered as detrimental precipitates in laves-phase strengthened steels.

In the as-rolled state of the KSX (KSY) material, MX-particles are small (<1μm) and are of relatively small amount. In MGQ coarsened particles (~5μm) in larger number were observed. By a comprehensive view on the composition analysis and processing parameters of the materials, it can be deduced that the higher volume concentration of this precipitate in MGQ was caused by the higher content of carbon and nitrogen and that they were further coarsened during the solution treatment cause of their stability against dissolution. It is also self-evident that with the super low C and N content in KUB, MX-particles were sparsely observed.

Besides MX-particles, La oxide was also discovered in Batches KUB (KUA) and MGQ (MDO). They appear as clusters in KUB (KUA) specimens and distributed evenly in MGQ (MDO) specimens what may be caused by the homogenization by solution treatment of MGQ (MDO). No La-oxide was observed in KSX specimens because of its super low La content. From previous and present investigation, no significant influence of LaO-particles on the thermo-mechanical properties of the materials and their precipitation kinetics is known.

4.2.2 Dislocation density

As discussed before, reduced dislocation density was thought to be the main reason for the inferior creep strength of the half-commercial materials (MGQ/MDO). In order to get a raw estimation of the difference in dislocation density between the laboratory and the half-commercial melts, hardness testing was applied to the materials. According to the literature review part, dislocation density is in proportion to the square value of the intrinsic hardness of a material. However, as the intrinsic hardness of a material also depends on several other factors such as solid solution state, precipitates etc. the precise value of dislocation density can not be calculated unless the other influencing factors are excluded. Although being aware of the fact that hardness is not a single matter of dislocation density, the dislocation densities have been calculated from the hardness measurements according to the N-G model, for the reasons that will be explained in the following.

Tab.6 Comparison of intrinsic hardness and dislocation density of the slab materials

Material	H_v (Intrinsic hardness) (±5%)	Dislocation density according to NG-model ($1/m^{-2}$)
MGQ	187	$(3.28\pm 0.16)\times 10^{13}$
KSX	203	$(3.75\pm 0.18)\times 10^{13}$
KUB	200	$(3.85\pm 0.19)\times 10^{13}$
KUB_005	180	$(3.03\pm 0.15)\times 10^{13}$

KUB_005 is a sample from batch KUB that has been solution treated at 1075°C for 40min (with subsequent air cooling) at our lab. It shows reduced intrinsic hardness compared to KUB in the as-received state. Since the sample is from the same batch, the matrix state should not be different. Thus the difference in hardness should be mainly caused by reduced dislocation density induced by solution treatment. In the same manner, the intrinsic hardness of MGQ material is smaller than that of KSX and KUB material.

The sheet materials exhibit higher intrinsic hardness (**Tab.7**) because of their production parameters (higher degree of deformation). Despite of this difference, similar to the slab materials, the half-commercial sheet material MDO exhibits lower intrinsic hardness compared to the laboratory materials (KUA and KSY). Comparing between the two laboratory materials, KSY exhibits higher intrinsic hardness than KUA. This higher intrinsic hardness indicating higher dislocation density is probably caused by the higher degree of deformation of the KSY material (2mm compared to 2.5 mm of KUA).

Tab.7 Comparison of intrinsic hardness and dislocation density of the sheet materials

Specimen	H_v (Intrinsic hardness) ($\pm$5%)	Dislocation density according to NG-model (1/m^{-2})
MDO	233	$(5.07\pm 0.25)\times10^{13}$
KUA	287	$(7.71\pm 0.39)\times10^{13}$
KSY	305	$(8.74\pm 0.44)\times10^{13}$

To obtain more information concerning the change of intrinsic hardness with different thermo-mechanical processing conditions, some pre-deformation and heat treatment experiments were conducted with MDO specimens. **Tab.8** lists the measured intrinsic hardness in accordance to different processing procedures.

MDO-700°C_10h has been annealed at 700°C for 10 hours. MDO-600°C_24h has been annealed at 600°C for 24 hours. Comparing these samples to the as-received state, it is evident that heat treatment actually had a strong effect on the intrinsic hardness. Since the specimens are all from the same melt, this great impact on intrinsic hardness should mainly be caused by the changes in dislocation density. As will be discussed later in the mechanical testing part, this strong recovery effect causes a great reduction of creep strength. Thus it should be regarded as an important factor in future production.

MDO-5% and MDO-10% are MDO samples with pre-deformations of 5% and 10% performed at room temperature before high temperature testing. Comparing their intrinsic hardness with the as-received state, 5% pre-deformation yields only small intrinsic hardness increase while 10% pre-deformation increases the hardness eminently.

It is obvious from these results that certain pre-deformation before mechanical testing can increase the intrinsic hardness of the material, and the higher the pre-strain, the larger the increase in intrinsic hardness. However, the pre-strain should be controlled within a certain range to prevent microstructural degradation like pore and crack formation.

Tab.8 Change of intrinsic hardness with different processing procedures

Specimen	H_v (Intrinsic hardness) (±5%)	Dislocation density according to NG-model ($1/m^{-2}$)
MDO	233	$(5.07 \pm 0.25) \times 10^{13}$
MDO-700°C_10h	202	$(3.83 \pm 0.19) \times 10^{13}$
MDO-600°C_24h	213	$(4.23 \pm 0.21) \times 10^{13}$
MDO5%	238	$(5.29 \pm 0.26) \times 10^{13}$
MDO10%	266	$(6.61 \pm 0.33) \times 10^{13}$

It should be emphasized that although only the intrinsic hardness values were compared in the previous discussion, the values hint at different dislocation densities. The three melts have similar chemical compositions with only slight differences. Therefore, the differences in intrinsic hardness discussed above should be mainly caused by different dislocation density.

4.3 Mechanical behavior of the sheet materials

4.3.1 Tensile testing

Fig.25 displays the room temperature tensile testing results of the three sheet materials. Obviously, MDO shows lower yield strength than the other two laboratory sheets, however, it has larger fracture strain what is attributable to the solution treatment which improves the ductility of the MDO material. On the other hand, comparison between KSY and KUA shows that KSY has higher yield and ultimate strength than KUA. The higher degree of deformation of the KSY material during production resulting in higher dislocation density may probably be the reason for this (2 mm KSY compared to 2.5 mm KUA).

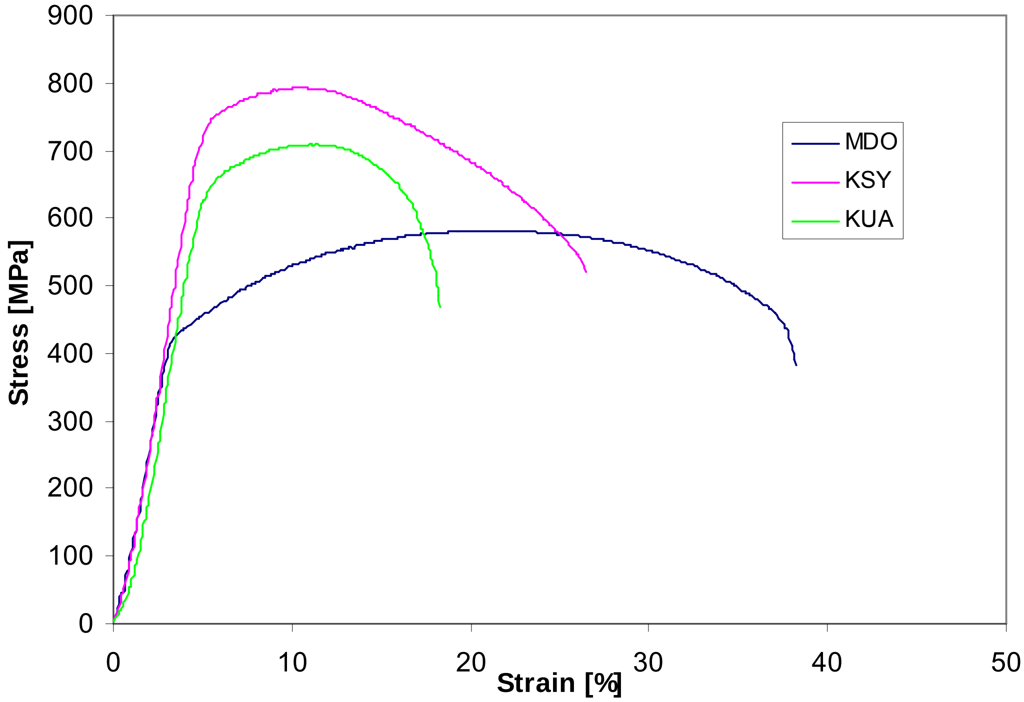

Fig.25 Room temperature stress-strain curves of the three sheet materials MDO, KSY and KUA

The 600°C tensile testing results were similar to that of the room temperature tests, with only larger fracture strain of the laboratory batches whose ductility increased because of the high testing temperature, what can be seen in **Fig.26**. Nevertheless, the strength of both laboratory materials drops quickly after the ultimate tensile strength is reached. Considering the initial microstructure of the three specimens and the fast strain rate during testing (which would not render enough time for the formation of precipitates), it is suspected that this relatively unstable behavior of the laboratory specimens might mainly be caused by a lack in strengthening Laves-phase precipitates in the as-received state.

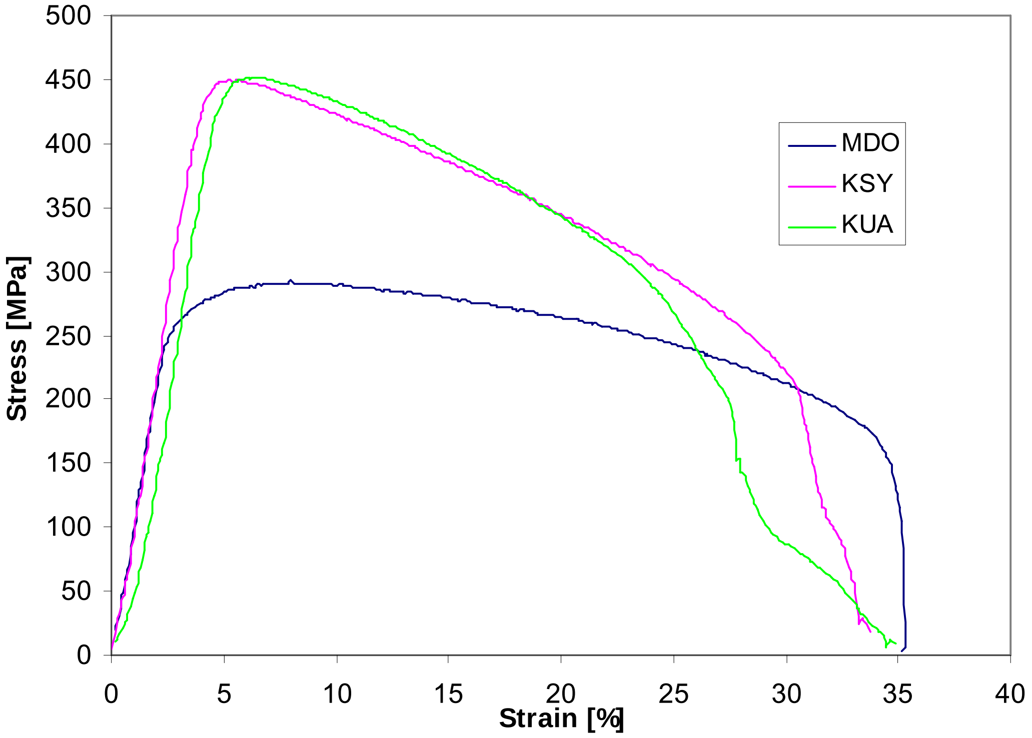

Fig.26 MDO, KSY and KUA tensile tested at 600°C

Tensile behavior of the three materials at 800°C (**Fig.27**) was almost similar to that at 600°C. Ductility of all materials increased remarkably, even up to 80% for the laboratory batches. With rising temperature, the difference in tensile strength between the laboratory and the half-commercial material reduced. This phenomenon should be ascribed to the increased dislocation activity caused by high temperature, in which dislocation density becomes less dominant during deformation.

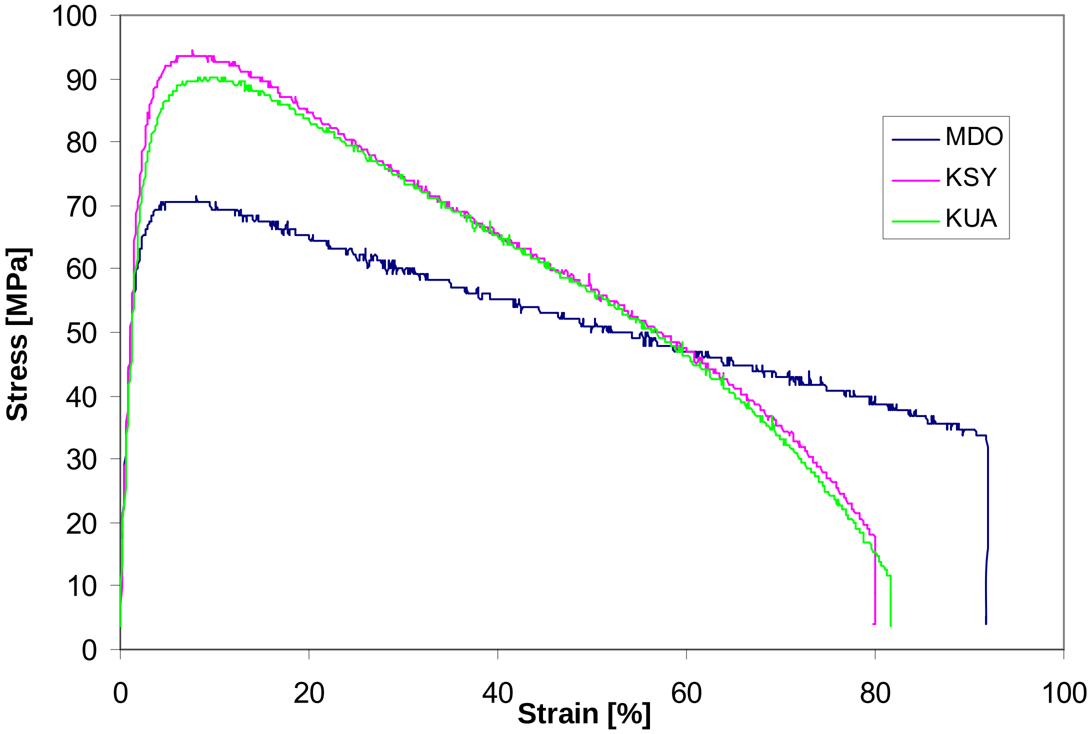

Fig.27 MDO, KSY and KUA tensile tested at 800°C

In an overall manner, since all the tensile tests were conducted at a comparatively fast strain rate of $10^{-3}s^{-1}$, the deformation mechanism at both 600°C and 800°C was dislocation dominated deformation. Therefore, higher dislocation density of the laboratory specimens yields higher yield and ultimate tensile strength than for the half-commercial MDO material. Meanwhile, because of the small amount of precipitates in the initial state and insufficient time for precipitation during fast tensile testing, the laboratory specimens showed unsustainable strength at further deformation after the ultimate tensile strength is reached. While for the MDO material, although it has comparatively low strength, its strength remained rather stable throughout the testing period thanks to the small and homogeneous laves-phase precipitates all over the matrix.

4.3.2 Stress relaxation testing

4.3.2.1 Evaluation of creep rates from stress relaxation testing

As discussed before each stress relaxation test comprises of two testing stages with different stress levels in order to cover wider stress ranges. For all the experiments that were conducted, the stresses of the two stages were chosen from three levels 150MPa, 175MPa and 250 MPa. The stress of the first stage can be either higher or lower than the stress of the second stage. That means, the experiment can be conducted in two ways: 1st stage: 150MPa, 2nd stage: 175MPa; or: 1st stage: 175MPa, 2nd stage: 150MPa. By conducting the stress relaxation stages in initial stress increasing way and in initial stress decreasing way, the influence of the first stage relaxation to the relaxation results of the second stage can be characterized.

For each stage, the data reduction method and calculation of the creep rate from the stress relaxation data is explained in the following. **Fig.28** shows exemplified SRT-curves in which smoothed and interpolated curves were deduced from the raw data curve using the software package Origin Pro8. With the interpolated 50 points, the creep rates have been calculated. The calculation comprises of two parts: First the strain change rate that reflects the change of machine strain, second the strain rate deduced from transfer from elastic to plastic specimen strain during stress relief. To calculate the machine strain rate, the equation stated in chapter “machine correction” $Y = 3.22 \cdot 10^{-10} \cdot x^4 - 1.78 \cdot 10^{-7} \cdot x^3 - 3.8 \cdot 10^{-5} \cdot x^2 + 6.83 \cdot 10^{-3} \cdot x - 1.7 \cdot 10^{-2}$ has been used. By substituting the interpolated stress value into x, the corresponding strain value Y can be deduced. The change of machine strain with time yields the first part of the creep rate. For the second part of the creep rate, the change of interpolated stress with time is calculated and divided by the Young’s modulus (167GPa for all the materials that were tested in this thesis). The creep rate results derived from these two parts comprise the total creep rate. **Tab.9** shows the example data for calculating the creep rate in the stress relaxation which is taken from the stress relaxation data of sample MDO_011.

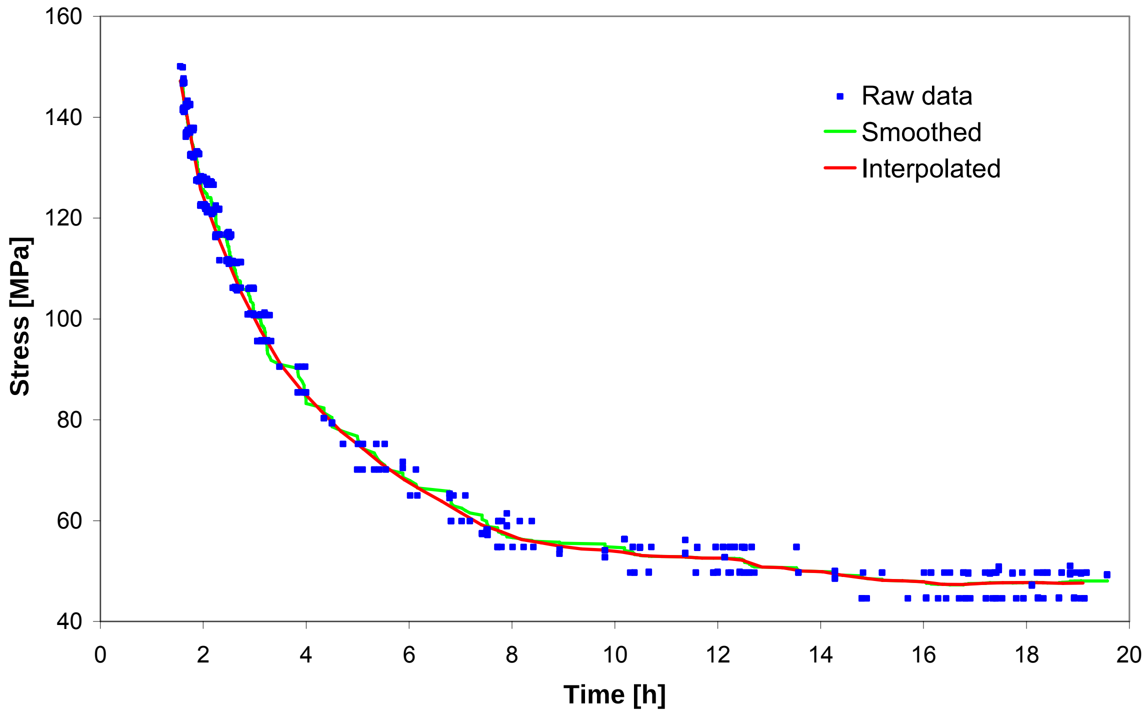

Fig.28 Smoothed and interpolated curve of the raw data calculated by the software package Origin Pro8 (MDO_011)

Tab.9 Example of calculating the creep rate from stress relaxation testing

Time [h]	Stress [MPa]	machine strain - corresponding to $\Delta\sigma$ [%]	Creep rate - corrected for Young's modulus [1/h]
1.559074829	147.23734	0.582598892	0.001737271
1.948843536	125.71856	0.515014368	0.000900841
2.28	116.35475	0.485238506	0.000788583
2.728380951	105.40000	0.449945535	0.00064882
3.118149658	97.70000	0.424702657	0.000585534
3.507918365	90.87793	0.40192121	0.000426414
3.897687072	86.00000	0.385330145	0.00037331
4.28745578	81.80000	0.370804857	0.00036936
4.677224487	77.71492	0.356432823	0.000286284
5.066993194	74.60000	0.345293002	0.000309114

4.3.2.2 Factors influencing the results of stress relaxation tests

As discussed before, stress relaxation tests can provide information concerning the creep strength of the tested material. **Fig.29** displays a Norton plot created from stress relaxation testing of the half-commercial batch MDO starting from a stress level of 150MPa at 600°C. All specimens were tested in the as-received state. The testing procedures are listed to the right. The dashed trend-lines represent the creep rates calculated from the stress relaxation part of each test, while the closed points (■,●) represent the creep rates deduced from the creep parts of the tests at 150MPa and 175MPa. Like it can be seen from the diagram, for MDO_010 the creep data calculated from the stress-relaxation tests correspond well with those derived from the constant load creep sections. This result proves that although stress relaxation and creep work in different ways, they both can render information concerning the creep rates and the results show good correspondence.

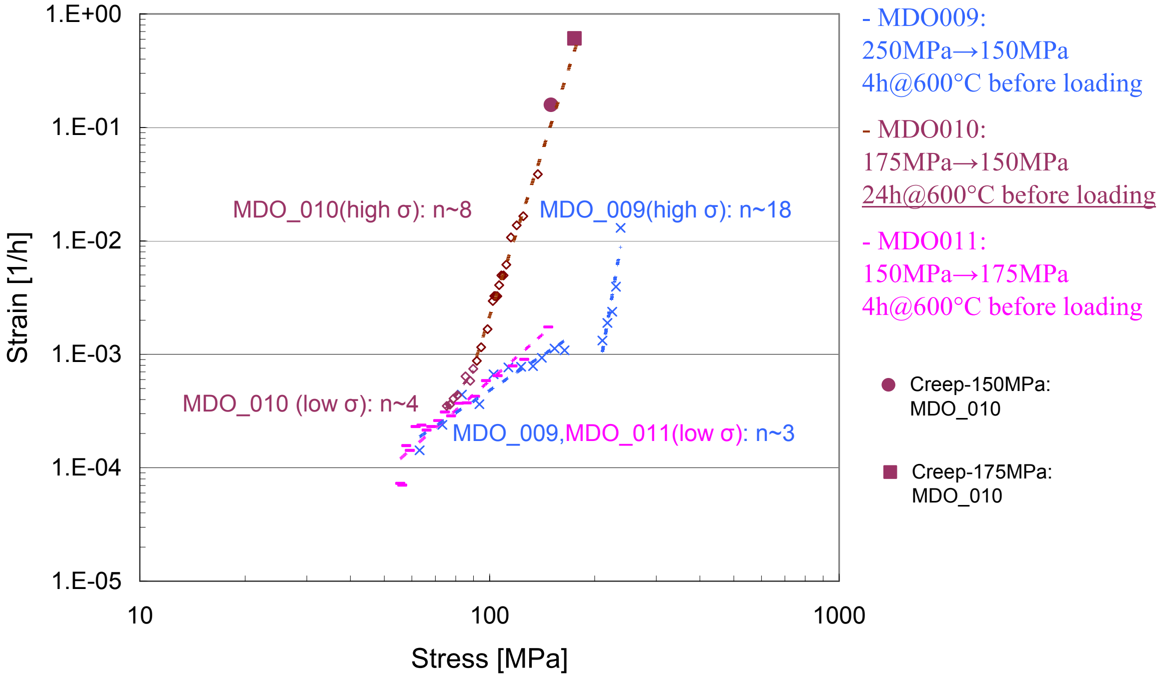

Fig.29 Norton plot of the MDO material
(Creep test @ 150 MPa; SRTs starting from 150+x MPa)

Besides, comparing the three results, it is found that for the relaxation testing procedure itself, the heating period before loading is very important. Specimen MDO_009 and MDO_011 had the same 4 hours heating period before loading. Their creep rate results correspond with each other. However, this was not the case for MDO_010. Its heating time has been 24 hours at 600°C before loading and accordingly, its creep rate increased in correlation to MDO_009 and MDO_011. As can be seen from **Fig.29**, although for both MDO_009 and MDO_010 the n values show the same trend from high stress regime to low stress regime, MDO_010 always exhibits higher creep rates at the same stress levels, especially in the high stress regime. This difference in creep rate may mainly be attributed to reduced dislocation density because of prolonged holding at 600°C before loading, which has been proved by indentation results in chapter 4.3.2.

On the other hand, for specimens MDO_009 and MDO_011, the testing sequence is different between the two specimens. The stress relaxation at 150MPa for MDO_009 was conducted at the second stage of the complete stress relaxation test, while for MDO_011, the 150MPa stress relaxation was at the first stage. However, despite of this difference, the results show good correlation. This fact shows that the testing sequence actually has minor influence to the stress relaxation behavior and several stages (or cycles) of stress relaxation has minor influence to the dislocation density change of the material. As for each stage, the work hardening and the recovery process would be in a balanced state and offset each other in the microstructural change of the material.

4.3.2.3 Relationship between dislocation density and creep rate

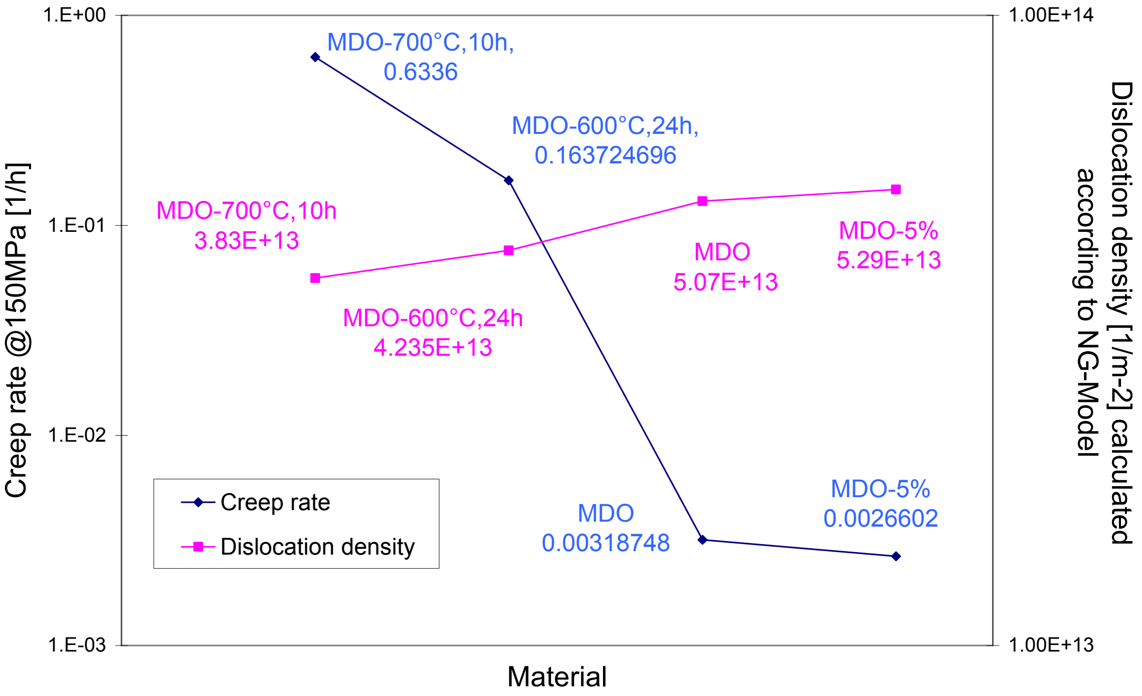

Fig.30 Correlation between dislocation density and creep rate for MDO material of differing thermo-mechanical treatment

Fig.30 shows the correlation between dislocation density and corresponding creep rate of the half-commercial batch MDO. Evidently the creep rate of the material decreases distinctively with the increase in calculated dislocation density. These results further prove that dislocation density plays an important role in attaining the creep strength of this steel and that its creep behavior can actually be changed by varying the processing procedures. Therefore, low dislocation density because of heat treatment should be a main cause for early failure in creep testing of the pre-commercial materials.

4.3.2.4 Correlation between stress relaxation, creep and tensile tests

Fig.31 presents strain rate versus stress results obtained from stress relaxation, creep and tensile tests. Like it can be seen, in an overall manner, either in stress relaxation, in creep or even in tensile testing, the half-commercial material MDO exhibits weaker high temperature mechanical performance than the laboratory batches KSY and KUA. All the materials show similar trend in stress relaxation, creep and tensile testing. The correspondence of the experiments shows that sufficient characterization of a material can be deduced from a short-term testing schedule and thus the mechanical behavior of the materials can be sufficiently quantified in terms of the effect of thermo-mechanical treatment history and corresponding microstructure. Nevertheless, long-term creep testing is still indispensable for creep strength investigation.

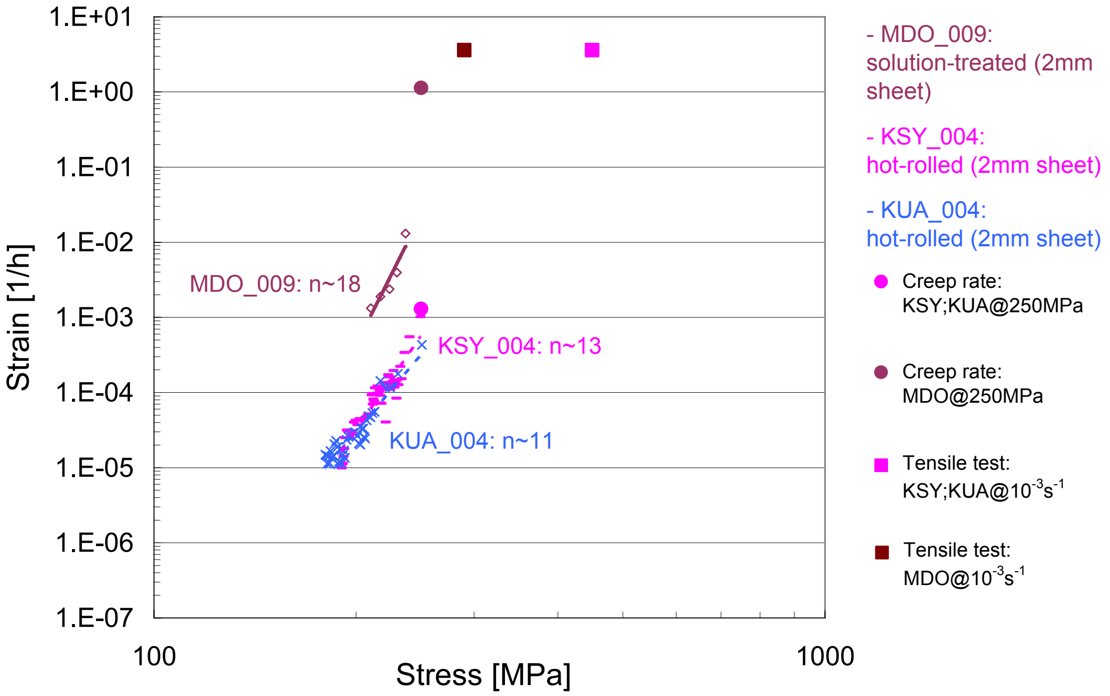

Fig.31 Comparison of stress relaxation, creep and tensile tests

4.3.2.5 Correspondence of the laboratory batches

As stated before, creep tests were performed with turned specimens from the slab materials in the past. To compare the creep behavior of the slab material from the creep tests and the sheet material from the stress relaxation tests, creep rate against stress was plotted for the four materials in **Fig.32**.

As discussed before, the two slab materials performed differently during the creep tests, what can be seen in **Fig.32**. The slab specimens from batch KSX exhibit lower creep rates than that of batch KUB. Considering the inhomogeneous grain structure of KSX differing hot-rolling and tempering parameters were suspected for the KSX material (chapter 4.3.1). The results of the sheet materials in stress relaxation testing emphasize this. The two sheet materials KSY and KUA from the corresponding melts of the slab materials exhibit similar creep behavior in the stress relaxation tests.

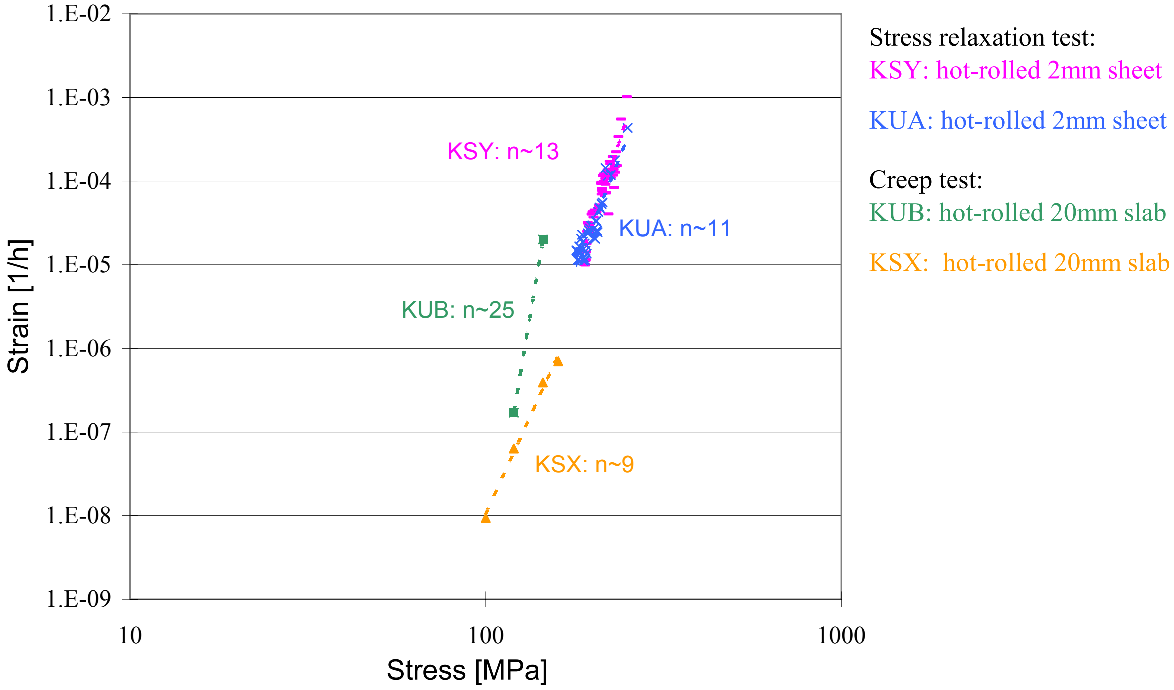

Fig.32 Comparison of slab and corresponding sheet materials of the two lab-melts

Since the laboratory materials have high creep strength, they hardly relax in the low stress regime. For this reason from SRT it is difficult to obtain creep rate data for the laboratory sheet materials in the low stress regime from SRT. On the contrary, the creep data of the slab materials was mainly gathered in the low stress regime for the investigation of long term application. Long term creep testing is time and material consuming. For these reasons only view data-sets were available from the slab materials. Especially for batch KUB, there were only 2 data-sets available for the calculation of the stress exponent. For this reason one has to be careful about the comparably high stress exponent of n~25. In the case of the KSX material the stress exponent has been calculated from 4 data-sets and seems to be reasonable and in good correspondence with the SRT data of the sheet materials. It has to be emphasized that long-term testing of the slab materials KUB and KSX has been performed in interrupted creep testing and for this reason without continuous displacement measurement. Specimen elongation has been measured by stopping the experiment, unloading and cooling down, releasing the samples from the machine and measuring the elongation by hand. This procedure can influence the materials behavior. But at least for KSX/KSY material the results gathered in both tests yield reasonable results. The behavior of batch KUB in long-term testing especially at high stress is still not clear, but seems to be linked to its microstructural difference to KSX, as can be deduced from the conformity of batches KUA and KSY.

5. Conclusion

The microstructural deviation of the half-commercial batches (MGQ and MDO) of brand new creep-resistant ferritic steel (Crofer 22H) in comparison to two laboratory melts is considered to be the main reason for its reduced creep strength at 600°C.

Grain size, precipitation behavior and dislocation density were the main issues considered in microstructural investigation. The grain size of the half-commercial batch was smaller (~100μm) than that of the laboratory batches (~500μm). This is considered to be one of the reasons that may have caused the weaker creep strength of the half-commercial specimen in high temperature creep testing.

The main strengthening Laves-phase precipitates were hardly found in the as-received state of the half-commercial slab material (MGQ), cause of the solution treatment that was performed after hot rolling. Besides, annealing experiments showed that precipitation behavior of the half-commercial material was inhomogeneous throughout the matrix and the lower the annealing temperature, the severer this inhomogeneity. The lack of strengthening precipitates in the as-received states and the following unusual precipitation behavior in comparison to high strength lab melts (KUA/KUB, KSX/KSY) are thought to be the reasons of early creep rupture of the half-commercial specimens at the initial stage of creep testing.

Dislocation density calculated by data from hardness testing using Nix and Gao’s model also proved that the half-commercial materials display lower dislocation densities than the laboratory batches. Creep testing results of sheet materials showed that dislocation density actually has a great influence on the creep rate. Increased dislocation density by pre-deformation improves the creep strength by reducing the creep rate.

High temperature tensile tests and stress relaxation tests were conducted in this work to characterize the materials’ mechanical properties at 600°C. The stress relaxation tests were conducted in a way that both creep rate at constant stress and stress relaxation at constant strain could be obtained. The correspondence of tensile, creep and stress relaxation data gave credible characterization of the mechanical properties.

In conclusion, the creep strength of this brand new creep resistant steel is highly related to its microstructure. The choice of processing parameters in future production should therefore be carefully deliberated considering measures to obtain an optimized microstructure and associated the optimum creep strength.

References

[1] A. Kostka, K.-G.Tak, etc: On the contribution of carbides and micrograin boundaries to the creep strength of tempered martensitic ferritic steels, Acta Materialia, 55 (2007), p. 539-550

[2] Y.Toda, H.Tohyama, etc: Influence of chemical composition and heat treatment condition on impact toughness of 15Cr ferritic creep resistant steel, JSME International Journal, 48 (2005), p.125-131

[3]http://www.gietech.be/LinkClick.aspx?fileticket=HJmiFOYi0RA%3D&tabid=111&mid=539

[4] Y.Murata, M.Morinaga, etc: Effect of carbon content on the mechanical properties of 10Cr-5W ferritic steels, Materials Science and Engineering A, 282 (2000), p.251-261

[5] Creep of metals and alloys, R.W Evans and B. Wilshire

[6] N.Fujita, K.Ohmura, etc: Changes of microstructures and high temperature properties during high temperature service of Niobium added ferritic stainless steels, Materials Science and Engineering A, 351(2003), p. 272-281

[7] V.Knezevic, J.Balun, etc: Design of martensitic/ferritic heat-resistant steels for application at 650°C with supporting thermodynamic modeling, Materials Science and Engineering A, 477 (2008), 334-343

[8] K.Yamamoto, Y.Kimura, etc: Design of Laves phase strengthened ferritic heat resisting steels in the Fe-Cr-Nb(-Ni) system, Materials Science and Engineering A, 329-331(2002), p.249-254

[9] J.Froitzheim, G.H.Meier, etc: Development of high strength ferritic steel for interconnect application in SOFCs, Journal of Power Sources, 178 (2008), p.163-173

[10] M.Hättestrand, H-O,Andren: Evaluation of particle size distribution of precipitates in a 9% chromium steel using energy filtered transmission electron microscopy, Micron, 32 (2001), 789-797

[11] Y.Hosoi, N. Wade, etc: Precipitation behavior of laves phase and its effect on toughness of 9Cr-2Mo ferritic-martensitic steel, Journal of Nuclear Materials, 141-143 (1986), p.461-467

[12] A.Aghajani, F. Richter, etc: On the formation and growth of Mo-rich Laves phase

particles during long term creep of a 12% Chromium tempered martensite ferritic steel, Scripta Materialia, 61(2009), p.1068-1071

[13] M.Hättestrand, H-O.Andren: Microstructural development during aging of an 11% Chromium steel alloyed with copper, Materials Science and Engineering A, 318 (2001), p.94-101

[14] M.Hättestrand, M.Schwind, etc: Microanalysis of two creep resistant 9-12% chromium steels, Materials Science and Engineering A, 250 (1998), p.27-36

[15] S.C.Bose, K.Singh, etc: Effect of thermal ageing on mechanical properties and microstructures of a standard G-X 12 CrMoVWNbN 1011 grade of cast steel for turbine casing, Materials Science and Engineering A, 476 (2008), p.257-266

[16] L.M.Lundin: Direct measurement of carbon solubility in the intermetallic (Fe,Cr)2(Mo,W) laves phase using atom-probe field-ion microscopy, Scripta Materialia, 34 (1996), p.741-747

[17] J.Pesicka, R.Kuzel,etc: The evolution of dislocation density during heat treatment and creep of tempered martensite ferritic steels, Acta Materialia, 51 (2003), p.4847-4862

[18] W.Nix, H.Gao: Indentation size effects in crystalline meterials: a law for strain gradient plasticity, J. Mech. Phys. Solids, 46 (1998), p.411-425

[19] S.Graça, R.Colaço, etc: Determination of dislocation density from hardness measurements in metals, Material Letters, 62 (2008), p.3812-3814

[20] G.Gottstein: Physical foundations of materials science, 2004

[21] J.K.L. Lai, C.A.P.Horton: Some effects of thermal aging and grain size on the creep behavior of a cast AISI type 316 stainless steel, Materials Science and Engineering, 54 (1982), p.285-289

[22] T.Fang, K.L.Murty: Grain-size-dependent creep of stainless steel, Materials Science and Engineering, 61 (1983), p.7-10

[23] A.Thorvaldsen: The intercept method—2.Determination of spatial grain size, Acta materialia, 45 (1997), p.595-600

[24] S.C. Tjong, Z.Y. Ma: Creep behavior of precipitation-hardened ferritic Fe-19Cr-4Ni-2Al alloy, Materials Letters, 56 (2002), p.59-64

[25] K.Kimura, Y.Toda etc: Creep strength of high chromium steel with ferrite matrix, 2nd International ECCC conference, April 21-23, 2009, EMPA, Dübendorf, Switzerland

[26] D.A.Woodford: Stress relaxation testing for creep design analysis of metals, ceramics and polymers, Creep and Fracture of Engineering materials and structures, 1997

[27] M.Yamashita: The stress-relaxation behavior of type 304 stainless steel, Int. J. Pres. Ves. & Piping, 42 (1990), p.203-216

[28] N.K.Sinha: Limitations of stress relaxation tests for determining stress dependence of strain rate at high temperatures, Scripta Materialia, 48 (2003), p.731-736

[29] J.H. Froitzheim: Ferritic steel interconnectors and their interactions with Ni base anodes in solid oxide fuel cells, Ph.D thesis, 2008

[30] G.R.Garces etc.: σ-phase precipitation in two heat-resistant steels----influence of carbides and microstructure, Scripta Materialia, 50 (2004), p. 651-654

[31] C.C. Hsieh etc.: Precipitation behavior of σ-phase in 19Cr-9Ni-2Mn and 18Cr-0.75Si stainless steels hot-rolled at 800°C with various reduction ratios, Material Science and Engineering A, 467 (2007), p.181-189

Abbreviation

SRT– Stress Relaxation Test

SEM – Scanning Electron Microscopy

TCP – Topologically Close Packed

APFIM – Atom Probe Field Ion Microscopy

TEM – Transmission Electron Microscopy

XRD – X-Ray Diffraction

P122/P92 – Martensitic Ferritic Creep Resistant Steel

MX/$M_{23}C_6$ – Carbonitrides; M: metal, X: C, N

ISE – Indentation Size Effect

LVDT – Linear Variable differential transformers

WQ – Water Quenching

Symbols

E – Young's modulus

T_m – Melting temperature

Cr_{eq} – Chromium equivalent

Ni_{eq} – Nickel equivalent

ε_0 – Total strain

ε_e – Elastic strain

ε_p – Plastic strain

σ – Stress

μ – Shear modulus

n – Stress exponent

b – Burger's vector

Ho – Intrinsic hardness

D_{Si}^{α} – Diffusion rate of Si in the ferritic matrix

Appendix

MX precipitates:

Morphology and chemical composition (MGQ-700°C, 1000h):

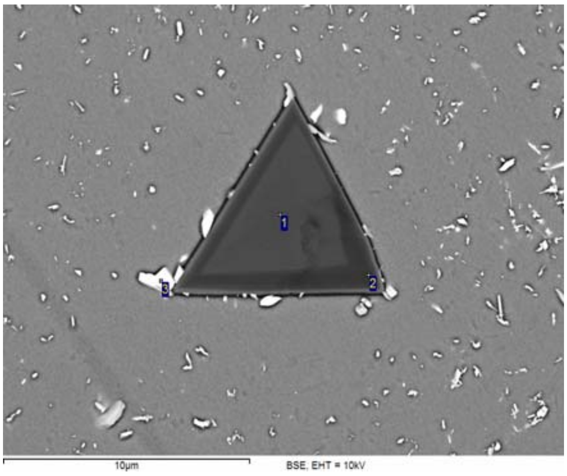

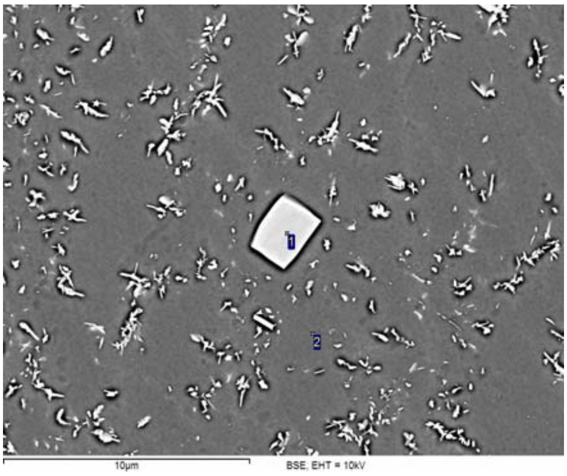

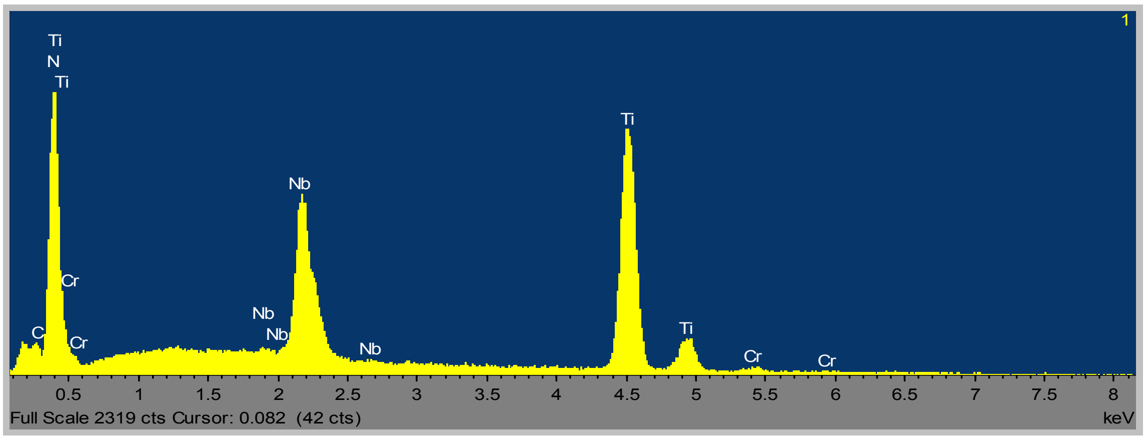

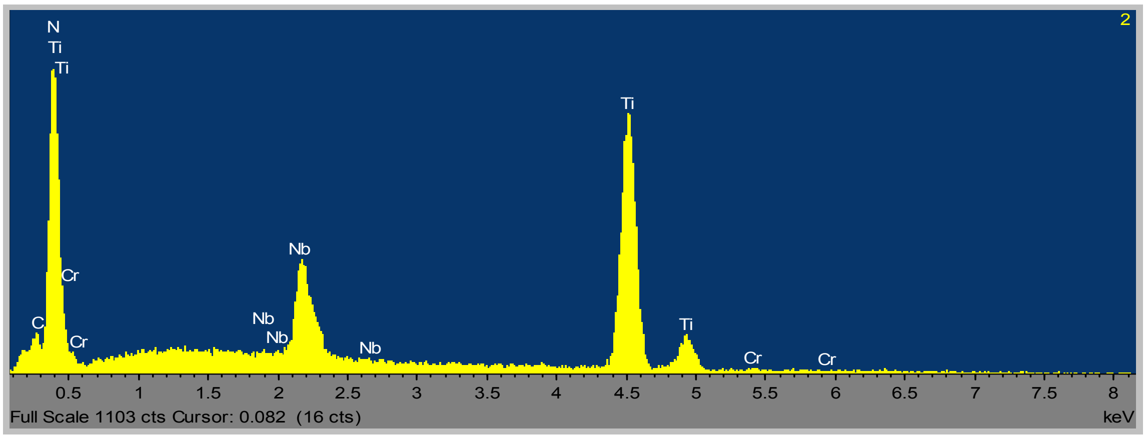

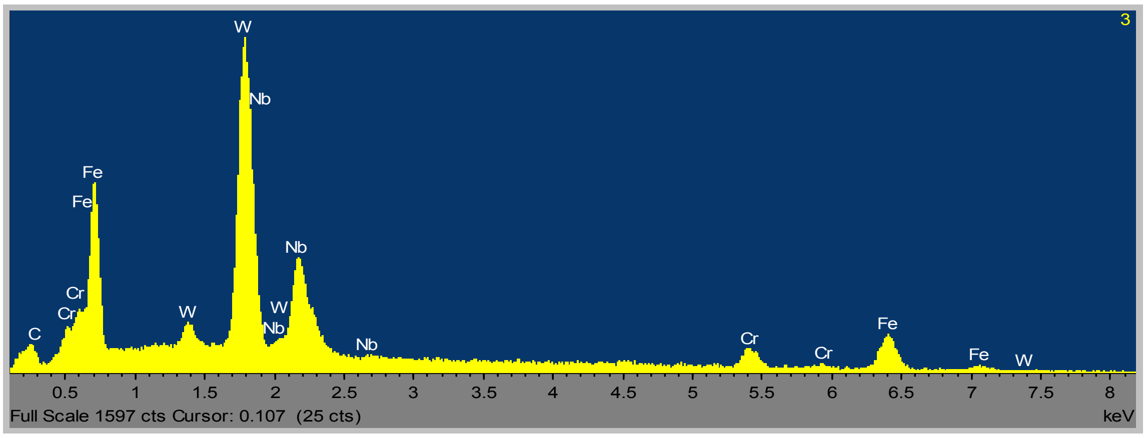

Size and distribution:

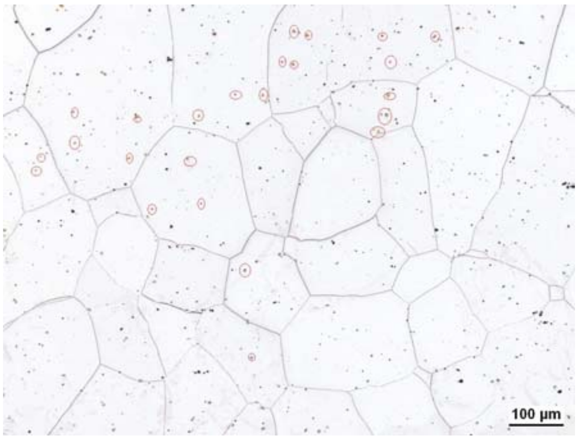

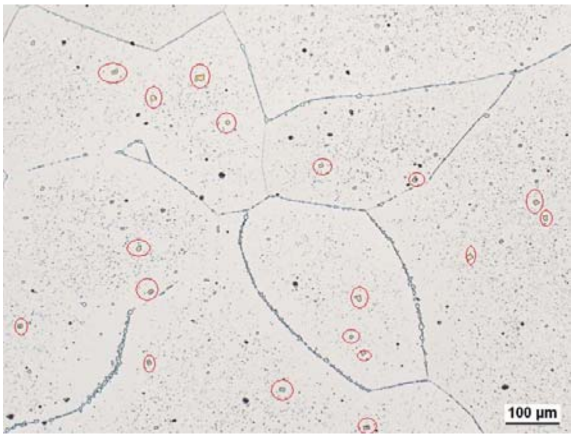

MGQ as-received

MGQ annealed (900°C, 1000h)

Laves-phase precipitates:

Annealing 700°C, 10h:

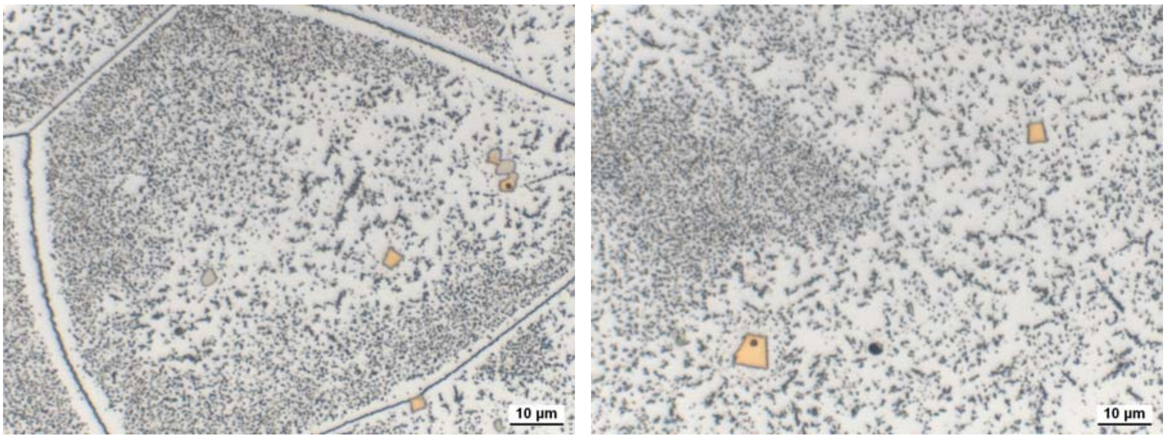

MGQ

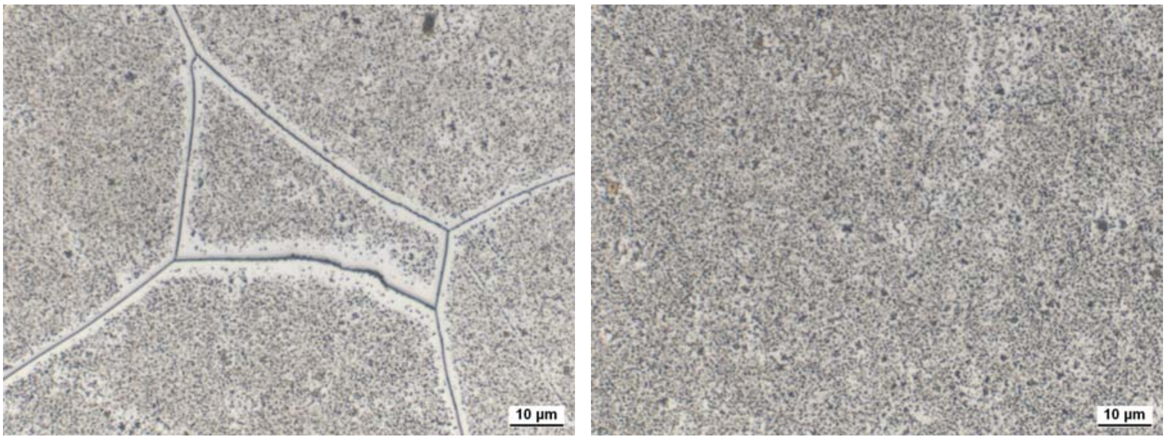

KSX

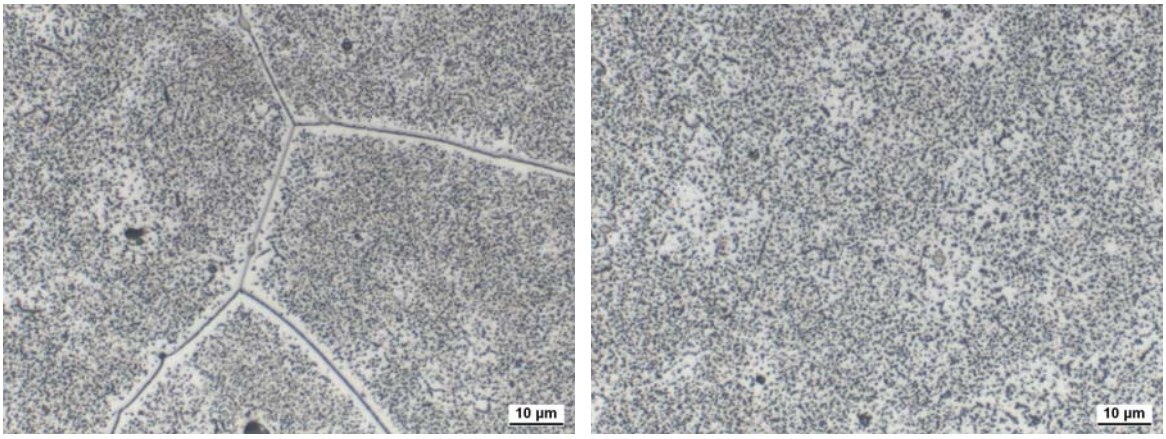

KUB

Annealing 700°C, 1000h:

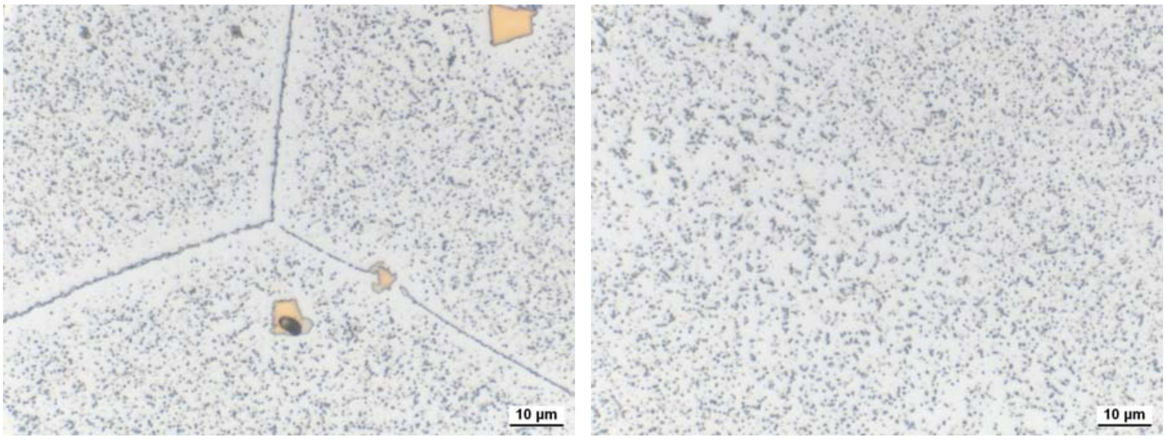

MGQ

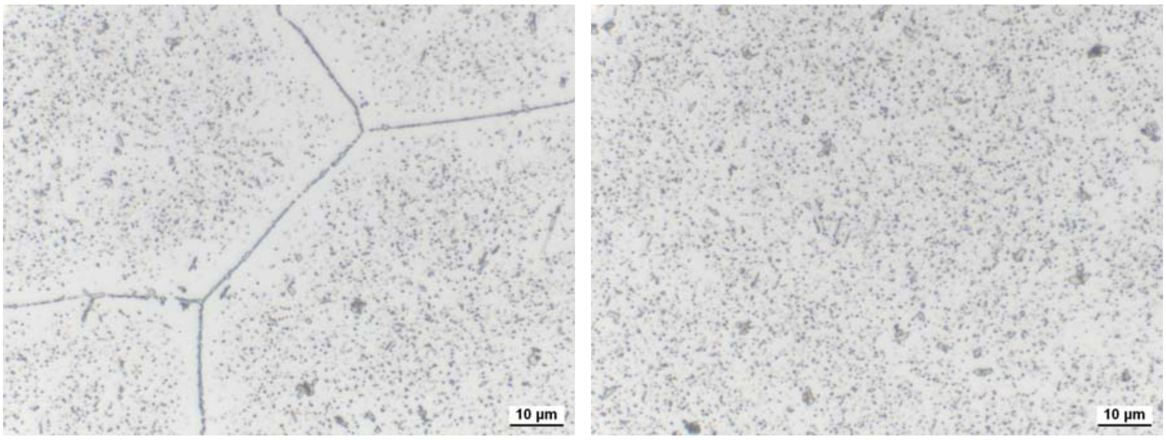

KSX

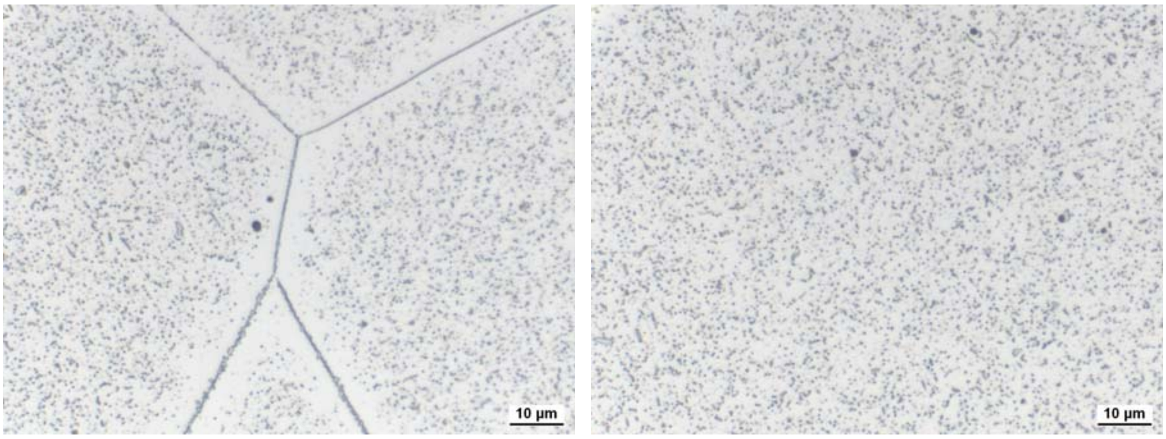

KUB